A Two-Dimensional Study of Coupled Grain Boundary Motion using Level Set Method

Anup Basak and Anurag Gupta*

Department of Mechanical Engineering, Indian Institute of Technology, Kanpur 208016, India

May 8, 2014

Abstract

The coupled motion of a closed non-circular grain boundary (GB) in a bicrystal, with both isotropic and anisotropic GB energies, is studied using the level set method. The kinetic relations, obtained within the framework of linear irreversible thermodynamics, govern the overall dynamics including normal motion (migration) of the GB, viscous sliding along the GB, and tangential motion of the grains which is geometrically coupled with the migration. The shape accommodation necessary to maintain coherency of relatively rotating and non-deforming grains is accomplished by allowing for diffusion along the GB. We solve the governing equations for the coupled motion to determine the shape and the misorientation evolution of an isolated GB under various constitutive assumptions. First, assuming both GB energy and kinetic coefficients to be isotropic, we study the interplay between kinetic coefficients for initially circular, near-circular, and non-circular GBs, as well as the role of stress and initial conditions on the GB dynamics. Next, we study the influence of anisotropy in GB energy, mobility, and geometric coupling for various combinations of parameters and initial conditions. Allowing for geometric coupling can in fact lead to distinctly different shapes than what are usually predicted on the basis of migration alone. Our numerical scheme provides a general framework to study these and other related problems of GB motion.

Keywords: grain boundary; coupled motion; level set method; anisotropic grain boundary energy; anisotropic kinetic coefficients.

*ag@iitk.ac.in (corresponding author)

1 Introduction

Grain boundary (GB) is a region in a crystalline solid which separates two crystals of identical phase but oriented differently. Grain boundaries move in the presence of driving forces provided by the stored energy in the grains, the stress field, the concentration gradient across the GB, the capillarity forces, etc. (cf. Ch. 3 in [1]). During GB motion, the atoms from the shrinking grain are transferred to the growing grain. Depending on the physical system, driving forces, and thermodynamical conditions, the relevant kinetics can be broadly categorized into two fundamental modes: (i) GB migration, where the GB moves along its normal direction (cf. Ch. 3 in [1]), and (ii) viscous GB sliding, where the two grains slide along the GB (cf. Sec. 12.8 of [2]). According to Read [3], when a bicrystal with a planar low angle tilt boundary is subjected to shear stress, the GB migration is accompanied by shear deformation in the adjacent crystals through a collective dislocation motion. On the other hand, Ashby's analysis in [4] clearly demonstrated that sliding between two grains is also accompanied by the normal motion of the GB. It has been observed that viscous sliding dominates over migration at high temperatures close to the melting point [4, 5]. In any case, GB migration and relative tangential motion of the grains are both coupled with each other. The kinetic laws formalizing this coupled motion were first given by Cahn and Taylor [6, 7]; the resulting motion is called the *coupled GB motion*. The tangential motion of a grain, when embedded inside another grain, results into a relative rotation between the grains. The grains themselves behave like rigid bodies in the absence of large external loading, allowing us to neglect their elastic and plastic deformation. The significance of grain rotation has been emphasized in several experimental studies related to plastic deformation in polycrystals with ultra fine and nano grains (cf. §7.2 of [8] and the references therein). For instance, the rotation leads to coalescence thereby increasing the average grain size. This naturally introduces a size effect on the mechanical properties of nanomaterials. The coupled GB motion can also provide insights into the recovery process in polycrystals during heat treatment, where subgrain rotation and coalescence are observed along with boundary migration (cf. §6.5.4 of [9] and the references therein).

The first experimental observation of a coupled GB motion is due to Li et al. [10], where the migration of low angle GBs was seen to be accompanied by a shear deformation of the neighboring grains. More recently, the coupling has been widely reported in the experiments on bicrystals with planar GBs (both low and high misorientation angles) under axial stress by Gottstein and coworkers [11, 12]. All of these experiments observe the region swept by the moving GB to be sheared with a change in the misorientation angle. These studies have also verified the analytical expressions for the geometric coupling factor derived by Cahn et al. [5]. A coupled GB motion has also been reported in nanocrystalline aluminium films in the presence of external tensile stress [13].

Cahn and Taylor [6] proposed a formalism to study the coupled motion in a bicrystal, with a circular columnar grain embedded inside a much bigger columnar grain. They introduced a pair of

kinetic relations which govern the normal motion of the GB and the relative rotation of the grains. This work was extended to non-circular GBs in [7], where the linear kinetic relations were obtained by first constructing a dissipation potential and then using the principle of minimum dissipation. The motion was however analyzed only for near-circular GBs. Verification of the coupled motion model has been achieved subsequently in several molecular dynamics (MD) [5,14–19] and phase field simulations [15,16,20]. These simulations have in addition provided useful information on the nature of GB energy and kinetic coefficients. Upmanyu et al. [16], in their MD simulations of the coupled motion in bicrystals with curved GBs, have observed rigid body rotation of the grains along with shrinkage of the inner grain. They also note that the grains stop rotating once the misorientation angle approaches the local minima of the GB energy. That the relative rotation of the grains is accompanied by viscous sliding along the GB has been shown in the MD simulations by Trautt and Mishin [14].

The molecular simulation methods, although irreplaceable for the purpose of investigating the constitutive character of the phenomena, are nevertheless computationally expensive limited by the maximum size of the grain and the overall simulation time. It is usually advantageous to use the information gathered from these simulations into the development of a macroscopic computational model. Techniques such as level set method [21] are often found to be very efficient in studying similar problems of boundary propagation. The Hamilton-Jacobi equation, which is the governing equation for the level set method, requires a prescription for the normal velocity. In the case of GB motion the normal velocity is given in terms of GB energy (and its derivatives), kinetic coefficients, stress field, and the shape of the boundary. The resulting framework is appropriate to study the evolution of arbitrary non-circular GBs with anisotropic GB energy and kinetic coefficients. To the best of our knowledge, the present work is first such level set based study of coupled GB motion. The level set method has been however extensively used to study recrystallization and grain growth in polycrystalline materials [22–28].

The article is organized as follows. In Section 2 we formulate the problem of coupled GB motion in the context of the present study including the kinetic relations and the constitutive specification for GB energy and kinetic coefficients. The derivation of the kinetic relations has been given in Appendix A. Our derivation is broader in scope; its extension to the three-dimensional case, and also for situations involving grain deformation, is conceptually straightforward. The simulation results are presented in Section 3. In Subsection 3.2 we study the coupled motion with isotropic GB energy and isotropic kinetic coefficients. In addition to emphasizing the role of misorientation dependence of the kinetic coefficients in the GB dynamics, we investigate the relative significance of these coefficients. We also compare the dynamics of a circular, near-circular, and a non-circular GB. Other results in this subsection include studying the role of viscous sliding and external stress in GB motion, and investigating the misorientation evolution as a dynamical system. In Subsection 3.3 the motion is studied for anisotropic GB energy and anisotropic kinetic coefficients. We divide our results

into three parts, first looking at the effect of anisotropic energy, keeping coefficients isotropic, followed by the combined effect of anisotropy in only energy and mobility, and finally allowing for anisotropy in geometric coupling factor. Whereas the anisotropy in mobility renders the faceted shape rounder, the presence of geometric coupling (not necessarily anisotropic) can lead to distinctively different shapes compared to those obtained without it. In all these cases we discuss the relevance of initial conditions, as well as stress, on the shape and the misorientation evolution. We conclude our study in Section 4.

We would like to emphasize here that the level set computations with anisotropic GB energy are in general very challenging. This is mainly due to the backward parabolic nature of the governing partial differential equation (PDE) [29]. Towards this end, the PDE is regularized by introducing a curvature dependent GB energy which in turn raises the order of the PDE, thereby introducing additional complexity in the numerical algorithm. It is therefore not surprising that very few level set studies in the context of anisotropic surface energies have appeared in the literature [30–32]. The scarcity of level set simulations for GB studies was also pointed out in a recent review by Rollett [33]. To fill the gap in the available literature for a systematic write-up on the implementation of level set methods to study GB motion, and also for making our presentation more complete, we have included a supplementary document on the numerical algorithm along with its verification using several classical problems like surface diffusion by the Laplacian of curvature, Wulff shape determination, and the normal migration of a GB with anisotropic energy.

2 Kinetic relations for GB motion

We study the coupled GB motion in a bicrystal where a grain in the form of generalized cylinder with arbitrary cross-section shape is embedded inside another generalized cylindrical grain of much larger size. The two grains, otherwise free of defects, are oriented differently. The coupled motion, which involves relative rotation of the grains in addition to the normal migration of the GB, is driven by the capillarity forces, the external stress along the GB, and the bulk stored energy [6, 7].

Relative rotation of the grains with a non-circular GB will necessarily require some shape accommodation mechanism so as to ensure the continuity of material points across the GB. The mechanisms can be drawn from one or more of the following possibilities: elastic deformation of the grains, plastic deformation of the grains, diffusion across the GB, and diffusion along the GB (see §12.8 of [2] for details). However, during a purely capillarity driven coupled GB motion, the stress values in the grains are such that no significant elastic deformation can take place (see Appendix B for an approximate analysis). For the same reason, the possibility of shape accommodation through plastic deformation of the grains can also be ruled out. In the absence of a concentration gradient across the GB, which is presently the case, the shape accommodation process has to be accompanied by diffusion along the GB. The latter is assumed to be driven by the non-uniform 'force' distribution on the GB, which

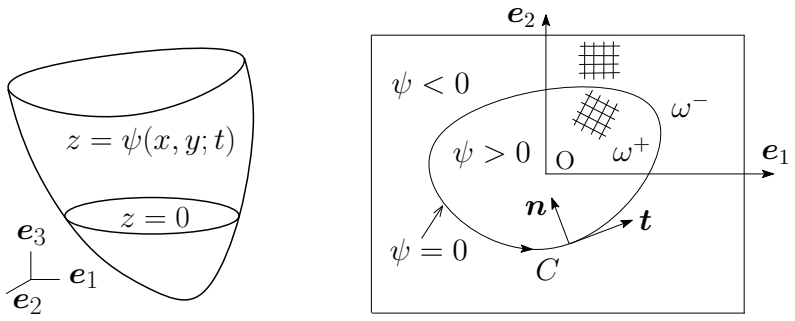

(a) (b)

Figure 1: (a) The zero level set (the curve with $z = 0$) embedded in a higher dimensional surface $z = \psi(x, y; t)$ where $\boldsymbol{x} = x\boldsymbol{e}_1 + y\boldsymbol{e}_2$. (b) A cross-section of the bicrystal having a cylindrical grain ω^+ surrounded by another cylindrical grain ω^- of much larger size.

arises due to the efforts put up by the grains to rotate along a non-circular boundary [7]. In our considerations, GB diffusion is driven by the relative rotation rate of the grains. This should be compared with the surface diffusion driven by the surface Laplacian of the curvature [34].

2.1 Kinematics

The GB geometry is as shown in Figure 1. We assume the GB to be a closed curve, denoted by C, such that there is a well defined normal at all of its points. It separates two grains ω^+ and ω^-. Let $\{\boldsymbol{e}_1, \boldsymbol{e}_2\}$ form a Cartesian basis with a fixed origin O. We consider a smooth function $\psi(\boldsymbol{x}, t)$ such that it is zero on the GB, positive within the inner grain ω^+, and negative in the outer grain ω^-, where $\boldsymbol{x} = x\,\boldsymbol{e}_1 + y\,\boldsymbol{e}_2$ is the position vector of a point in the domain and t represents time. The normal $\boldsymbol{n}$ and the normal velocity V, associated with the GB, are defined as (evaluated at $\psi = 0$)

$$\boldsymbol{n} = \frac{\nabla\psi}{||\nabla\psi||} \text{ and} \tag{2.1}$$

$$V = -\frac{\partial\psi/\partial t}{||\nabla\psi||}, \tag{2.2}$$

respectively, where ∇ is the gradient operator and $||\cdot||$ is the Euclidean norm of a vector. Assuming that the unit tangent vector $\boldsymbol{t}$ is directed in the direction of the increasing arc length along C, it can be written as

$$\boldsymbol{t} = \frac{\partial\psi/\partial y}{||\nabla\psi||}\boldsymbol{e}_1 - \frac{\partial\psi/\partial x}{||\nabla\psi||}\boldsymbol{e}_2. \tag{2.3}$$

The curvature κ of the GB is defined by

$$\kappa = -\nabla \cdot \boldsymbol{n}. \tag{2.4}$$

Neglecting rigid body translation, the material velocity $\boldsymbol{v}$ of the rigid motion of the grains can be expressed as (cf. Chs. 10 and 11 in [35])

$$\boldsymbol{v} = \dot{\boldsymbol{R}}\boldsymbol{R}^T\boldsymbol{x}, \tag{2.5}$$

where $\boldsymbol{R}$ is the rotation tensor, the superscript T stands for the transpose of a tensor, and the superposed dot represents the time derivative. Without loss of generality we can assume the outer grain to remain stationary, i.e. $\boldsymbol{R}^- = \mathbf{1}$ and $\boldsymbol{v}^- = \mathbf{0}$. The rotation tensor for ω^+ can then be written as (rotation occurs in the direction of the tangent vector)

$$\boldsymbol{R}^+ = \cos\theta\, \boldsymbol{e}_1 \otimes \boldsymbol{e}_1 - \sin\theta\, \boldsymbol{e}_1 \otimes \boldsymbol{e}_2 + \sin\theta\, \boldsymbol{e}_2 \otimes \boldsymbol{e}_1 + \cos\theta\, \boldsymbol{e}_2 \otimes \boldsymbol{e}_2, \tag{2.6}$$

where θ is the misorientation angle between ω^+ and ω^-, and $\otimes$ denotes the dyadic product. The relative tangential velocity, defined by $U_{\tan} = (\boldsymbol{v}^+ - \boldsymbol{v}^-) \cdot \boldsymbol{t}$, reduces to

$$U_{\tan} = -\dot{\theta}\boldsymbol{x} \cdot \boldsymbol{n}. \tag{2.7}$$

The normal component of the material velocity, given by $v_n = \boldsymbol{v} \cdot \boldsymbol{n}$, is discontinuous at the GB. It takes the form

$$v_n^+ = (\dot{\boldsymbol{R}}^+)(\boldsymbol{R}^+)^T\boldsymbol{x} \cdot \boldsymbol{n} = \dot{\theta}\boldsymbol{x} \cdot \boldsymbol{t} \text{ and } v_n^- = 0 \tag{2.8}$$

for material points approaching the GB from the inside and the outside, respectively.

2.2 Kinetic relations

The kinetic relations for the coupled GB motion are given by (see Appendix A for derivation)

$$V = \frac{MS}{S + M\beta^2} f_n - \frac{M\beta}{S + M\beta^2}(\boldsymbol{x} \cdot \boldsymbol{n})\dot{\theta} \text{ and} \tag{2.9}$$

$$\dot{\theta} = \frac{-\oint_C \frac{M\beta}{S+M\beta^2} f_n (\boldsymbol{x} \cdot \boldsymbol{n}) ds - \oint_C f_s ds}{\oint_C \frac{1}{S+M\beta^2}(\boldsymbol{x} \cdot \boldsymbol{n})^2 ds - \oint_C \frac{1}{2D_m}\left(R^2 - \overline{R^2}\right)^2 ds}, \text{ where} \tag{2.10}$$

M - GB mobility (see Appendix A.3 and Subsection 2.3),
S - viscous sliding coefficient (see Appendix A.3 and Subsection 2.3),
β - geometric coupling coefficient (see Appendix A.3 and Subsection 2.3),
D_m - diffusion mobility (see Appendix A.2),
$f_n = [\![\boldsymbol{E}]\!]\boldsymbol{n}\cdot\boldsymbol{n} + f_{\text{curv}}$ is the driving force for normal GB motion (see Appendix A.2), $[\![\boldsymbol{E}]\!] = (\boldsymbol{E}^+ - \boldsymbol{E}^-)$,
$f_s = (\boldsymbol{E}^+\boldsymbol{n} \cdot \boldsymbol{n})\boldsymbol{x} \cdot \boldsymbol{t} + \tau\boldsymbol{x} \cdot \boldsymbol{n} + \partial\gamma_c/\partial\theta$ is part of the driving force for tangential motion between the grains (see $(\text{A.21})_2$),
$\boldsymbol{E}$ - bulk Eshelby tensor (see Appendix A.2),
τ - tangential stress along the GB,

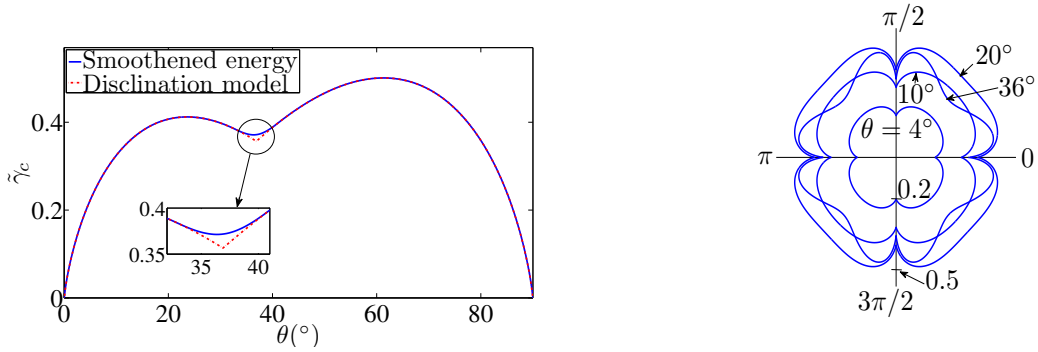

(a) (b)

Figure 2: (a) Isotropic GB energy. The inset shows a zoomed picture of the sharp cusp and its smoothening (using cubic splines) in the neighborhood of the cusp angle. (b) Polar plot of the anisotropic GB energy for varying misorientation angles.

γ_c - GB energy without the curvature dependent part (see (A.14)),
f_{curv} - capillarity force at the GB (see (A.16)),
R - radial distance of the GB from the origin O,
$\overline{R^2}$ - mean square radius of the GB (see Equation (A.9)), and
ds - infinitesimal arc length along C,
The above relations are valid for $M > 0$ and $S \geq 0$.

Similar kinetic relations for non-circular closed GBs were first derived by Taylor and Cahn in [7] by minimizing a dissipation potential. Our derivation in Appendix A follows an alternative approach where the kinetic relations are postulated directly from the dissipation inequality within the framework of linear irreversible thermodynamics.

2.3 Constitutive relations

The coefficients M, S, and β in the above equations as well as the GB energy (denoted by γ_c), which appear in the expressions for the driving forces, are all assumed to depend on the relative misorientation between the two grains and the inclination of the GB. The former is independent of the position, due to the absence of any defects within individual grains, and evolves in time according to (2.10) above. The inclination of the GB, denoted by ϕ (such that $\cos\phi = \boldsymbol{n} \cdot \boldsymbol{e}_1$), evolves according to a partial differential equation derivable from (2.9) [36]. In the present section we collect constitutive prescriptions for γ_c, M, S, and β to be used in our numerical simulations. All the relations have been written for crystalline grains with four-fold symmetry in the two-dimensional plane.

GB energy (γ_c) An expression for GB energy is derived from the disclination model of GB, where the GB is modeled as an array of disclination dipoles [37, 38]. The energy obtained is valid for the entire range of misorientation, unlike the energy calculated from a dislocation based model of GB. The disclination model can also account for finite number of cusps in the GB energy. We consider a model where a general GB is assumed to be composed of alternating segments of two special boundaries at angles θ_A and θ_B, delimited by partial disclinations of strength $\pm(\theta_B - \theta_A)$ [38]. The GB energy for $\theta_A \leq \theta \leq \theta_B$ and all ϕ is given by

$$\gamma_c(\theta,\phi) = \begin{cases} E(\phi)(\theta-\theta_A)\left[A_c(\phi) - \ln(\theta-\theta_A)\right], & \text{for } \theta_A \leq \theta \leq \theta_c, \\ E(\phi)\left[(\gamma_1-\gamma_2)\left(1-\frac{\theta-\theta_c}{\theta_B-\theta_c}\right) + (\theta_B-\theta)\left(A_c(\phi) - \ln(\theta_B-\theta)\right)\right], & \text{for } \theta_c \leq \theta \leq \theta_B, \end{cases} \tag{2.11}$$

where

$$E(\phi) = \gamma_0(|\cos\phi| + |\sin\phi|), \tag{2.12}$$

$$A_c(\phi) = \ln\left(\frac{\exp(3/2)(\theta_B-\theta_A)}{2\pi}\right) - \frac{|\sin 2\phi|}{2} - \frac{|\cos\phi|\ln|\cos\phi| + |\sin\phi|\ln|\sin\phi|}{|\cos\phi| + |\sin\phi|} \tag{2.13}$$

(see Chs. 11 and 12 in [3]), and γ_0 is a material constant. For a $\langle 100\rangle$ symmetric tilt boundary in cubic crystals, $\theta_A = 0$ and $\theta_B = \pi/2$. In (2.11) θ_c represents the misorientation angle where γ_c has a cusp; we take it as 36.9°. The term γ_1 is given by γ_c, evaluated at θ_c, using the first expression in (2.11), whereas γ_2, also evaluated from γ_c at θ_c, but after replacing $\theta - \theta_A$ by $\theta_B - \theta$ in the first expression for γ_c in (2.11). It is to be noted that (2.11) coincides with the Read-Shockley energy [3] in the small misorientation range ($\theta < 15°$). For an isotropic GB energy, E and A_c are both taken to be constants given by γ_0 and the first term on the R.H.S. of (2.13), respectively.

Figure 2(a) shows that the GB energy given by (2.11), and non-dimensionalized as $\tilde{\gamma}_c = \gamma_c/\gamma_0$, has a sharp cusp (the red broken curve) at θ_c, making $\tilde{\gamma}_c(\theta)$ non-differentiable at that point. The differentiability is however required for the well-posedness of (2.9) and (2.10) at all values of θ. We circumvent this problem by smoothening the energy with a cubic spline in the neighborhood of θ_c, as shown by the solid blue line in the figure. Although this allows us to solve (2.9) and (2.10) in the entire misorientation range, we can expect to miss the physical effect of cusp in our simulations. For instance we fail to capture the freezing of rotation exactly at the cusp angle, observed frequently in MD simulations [14, 16], but instead find the fixed point at an angle slightly away from θ_c. In Figure 2(b) we provide polar plots of the GB energy (2.11) for different misorientation angles with cusps appearing at discrete inclination angles. These plots clearly show that, at higher misorientation angles, additional local minima appear at inclination angles $\phi = \pi/4,\ 3\pi/4,\ 5\pi/4$, and $7\pi/4$. The appearance of additional minima in the GB energy can be attributed to the fact that, for high misorientation angles, grain boundaries corresponding to $\phi = 0$ and $\phi = 45°$ have equivalent dislocation structure [3, 39]. For small misorientation angles ($\theta < 15°$), since $\max(|A_c(\phi)|) \ll |\ln\theta|$ for $0 \leq \phi \leq 2\pi$, GB energy reduces to a decoupled function of θ and ϕ. That this is not so at larger misorientation angles leads to some very interesting observations while solving the problem of

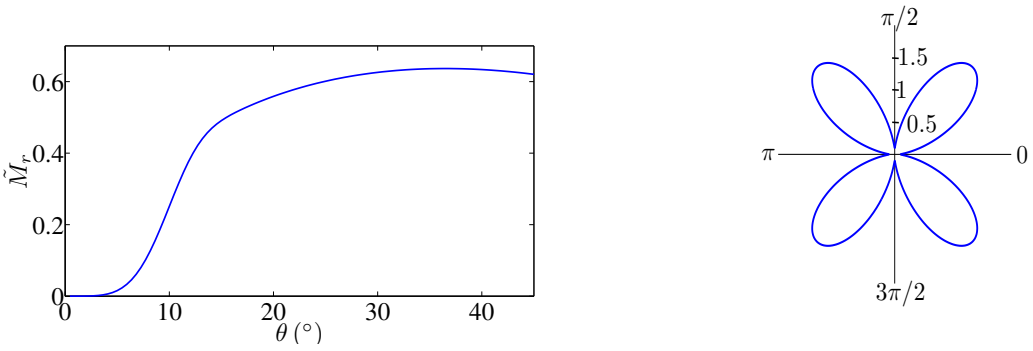

(a) (b)

Figure 3: (a) Misorientation dependent non-dimensional reduced mobility. (b) Polar plot for mobility $\tilde{M}_2(\phi)$ with $\alpha_M = 0.9$.

coupled GB motion, for instance the widening and the shortening of the corner region. Additionally, we need a twice-differentiable $\tilde{\gamma}_c$ for all ϕ. Towards this end we have smoothened the cusps which appear in Figure 2(b) using cubic splines. The arbitrary smoothening can be justified by assuming the grains to be above the thermal roughening temperature [40].

Mobility (M) We assume the constitutive relation for mobility as a decoupled function of θ and ϕ:

$$M(\theta, \phi) = M_0 \tilde{M}_1(\theta) \tilde{M}_2(\phi), \tag{2.14}$$

where M_0 is a constant coefficient (discussed further towards the end of the present section),

$$\tilde{M}_1(\theta) = 1 - \exp\left(-B(\theta/\theta_0)^A\right), \text{ and} \tag{2.15}$$

$$\tilde{M}_2(\phi) = 1 - \alpha_M \cos 4\phi. \tag{2.16}$$

The overall non-dimensional mobility is defined as $\tilde{M} = M/M_0$. For an isotropic mobility function, we take $\tilde{M} = \tilde{M}_1(\theta)$.

Equation (2.15) has been proposed by Humphreys [41] as a phenomenological model for mobility during grain growth. The parameters A, B, and θ_0 are taken as 4, 5, and 15° respectively [41]. Our choice of misorientation dependence of the mobility, illustrated in Figure 3(a) with the reduced mobility $\tilde{M}_r(\theta) = \tilde{M}_1(\theta)\tilde{\gamma}_c(\theta)$, is in good qualitative agreement with Figure 13 of [14] obtained by MD simulations of coupled GB motion. On the other hand, in deciding the inclination dependence of GB mobility we follow Kazaryan et al. [42] who proposed (2.16) for GBs in four-fold symmetric crystals, where α_M is a phenomenological parameter taken as 0.9 [42], see Figure 3(b). While studying the shrinkage of an isolated GB using (2.16) they observed that, when both GB energy and mobility are anisotropic (with four-fold symmetry), an initially circular GB remains almost circular throughout the evolution. The phenomenon was confirmed in the MD simulations [43, 44].

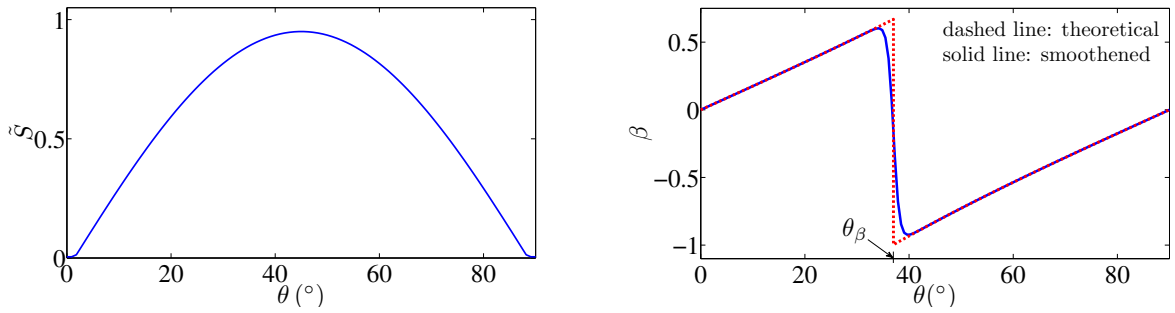

(a) (b)

Figure 4: (a) Non-dimensional sliding coefficient. (b) Isotropic coupling factor.

Sliding coefficient (S) To the best of our knowledge, a functional form for the sliding coefficient $S(\theta, \phi)$ is unavailable in the literature. For the lack of relevant data on inclination dependence, we assume S to be only θ dependent. Following the data for GB sliding presented by Gifkins [45] and Watanabe [46], we formulate the sliding coefficient as

$$S(\theta) = S_0 \, \tilde{S}(\theta), \tag{2.17}$$

where S_0 is a constant coefficient, whose order has been estimated towards the end of this section, and

$$\tilde{S}(\theta) = \max((\sin 2\theta - 0.05), 0.005) \tag{2.18}$$

is the non-dimensional sliding coefficient. The graph for (2.18) in Figure 4(a) shows that sliding can occur more easily at high angle boundaries compared to those with small misorientation angles. This is consistent with the results of [5].

Coupling factor (β) Following Cahn et al. [5] we assume the form of isotropic coupling factor $\beta(\theta)$ as

$$\beta(\theta) = \begin{cases} 2\tan(\theta/2), & \text{if } 0 \le \theta \le \theta_\beta, \\ -2\tan(\pi/4 - \theta/2), & \text{if } \theta_\beta < \theta \le 90^\circ, \end{cases} \tag{2.19}$$

where θ_β is a material constant denoting the misorientation angle at which mode switching occurs. This relation has been subsequently verified using MD simulations [5, 14, 47], phase field simulations [20], and experiments [11,12]. The coupling factor in (2.19) is discontinuous at θ_β, which disturbs the well-posedness of the differential equations (2.9) and (2.10). To avoid this shortcoming, we assume the transition of β from one mode to another to occur smoothly within a narrow range of θ ($\sim 6^\circ$) in the neighborhood of θ_β, see Figure 4(b). Even from a practical viewpoint, this assumption is not completely arbitrary. Both MD simulations and experiments predict the mode transition angle only

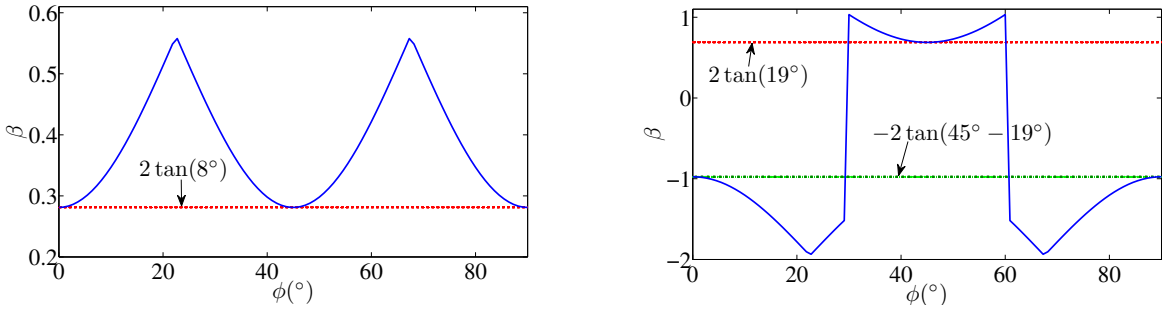

(a) (b)

Figure 5: Plot for anisotropic coupling factor $\beta(\theta, \phi)$ with (a) $\theta = 16°$ and (b) $\theta = 38°$.

within a range of around 6°, see §8 in [14] and the discussion in [12]. Following the cited studies, we take θ_β to be 36°.

The anisotropic nature of the coupling factor has been investigated recently by Trautt et al. [14] using MD and phase field simulations. Interestingly they find the coupling factor to be discontinuous only within a range of inclination angles. Outside of this range it remains a continuous function of the misorientation. Based on their simulation data we have constructed the following functional form for $\beta(\theta, \phi)$:

$$\beta(\theta,\phi) = \begin{cases} 2\tan(\theta/2)(2 - |\cos 4\phi|), & \text{for } 0 \le \theta \le \theta_\beta \text{ and } 0 \le \phi \le 90°, \\ 2\tan(\theta/2)(2 - |\cos 4\phi|), & \text{for } \theta_\beta < \theta \le 90° \text{ and } 30° \le \phi \le 60°, \\ -2\tan(\pi/4 - \theta/2)(2 - |\cos 4\phi|), & \text{for } \theta_\beta < \theta \le 90° \text{ and } \{0 \le \phi < 30° \text{ or } 60° < \phi \le 90°\}. \end{cases} \tag{2.20}$$

A graph of the anisotropic coupling factor with respect to inclination angles is shown in Figures 5(a) and 5(b) for $\theta = 16°$ and 38°, respectively. These plots are in good qualitative agreement with Figures 20 and 21 of [15].

Non-dimensional parameters r_1 and r_2 We introduce two non-dimensional parameters r_1 and r_2 as

$$r_1 = \frac{S_0}{M_0}, \text{ and } r_2 = \frac{R_0^2 M_0}{D_m}, \tag{2.21}$$

where R_0 is a characteristic length scale related to the embedded grain size. Both of these present themselves naturally if we write the governing differential equations (2.9) and (2.10) in a non-dimensional form. Whereas the former represents the relative magnitude of viscous sliding and mobility, the latter provides a ratio of a geometrical length scale (provided by R_0) and a material length scale (obtained from $\sqrt{D_m/M_0}$). In the following we motivate our choice for values of r_1 and r_2 to be used in the numerical simulations. We start by noting that the GB diffusivity $D_{GB} \sim 10^{-9}\text{m}^3/\text{Ns}$ near melting point T_m [48]. We use this value in the microscopic model of the viscous sliding coefficient

for high angle GBs, given by $S_0 \approx bD_{GB}\delta_{GB}/k_BT$ [4], to get $S_0 \approx 2.2 \times 10^{-8}\text{m}^3/\text{Ns}$, where Burgers vector $b = 0.36\text{nm}$ (for Cu), GB thickness $\delta_{GB} = 1\text{nm}$, Boltzmann constant $k_B = 1.38 \times 10^{-23}\text{J/K}$, and $T = 1200\text{K}$. On the other hand we estimate $M_0 \approx 1.2 \times 10^{-7}\text{m}^3/\text{Ns}$ using Figure 12 of [14] and noting that $\gamma_c \approx 0.85\text{N/m}$ for high angle isotropic boundaries in Cu. Consequently we obtain $r_1 \approx 0.2$ from high angle GB data close to the melting point. This value of r_1 is calculated at favorable conditions for sliding. However, while sliding becomes increasingly difficult as the temperature is decreased below T_m, the tangential motion as well as the normal GB motion remain active [5]. This will result into a r_1 less than 0.2. In the present study we consider values of r_1 between 0.01 and 1. The range of values given by $r_1 > 0.2$ will accommodate cases where the expression for S_0 contains a constant pre-multiplier greater than 1 (see e.g. Equation (7) in [4], where the multiplier is 8 for a non-planar GB).

To evaluate r_2 we need to first estimate a value for D_m. To this end, we recall a recent study on sliding accommodated by GB diffusion for a hexagonal GB [49]. Comparing (A.23) with Equation (15) in [49] we take $D_m = D_{GB}\delta_{GB}v_a/k_BT$, where v_a (the atomic volume) is calculated using an atomic radius of 0.128nm. With the obtained expressions for S_0 and D_m, we can write

$$r_2 = \frac{1}{r_1}\frac{R_0^2}{\ell^2}, \tag{2.22}$$

where $\ell = \sqrt{v_a/b}$ is a length scale depending on the lattice constant. Using $R_0 = 10\text{nm}$ we get $r_2 = 4.1 \times 10^3/r_1$. It should be noted that (2.22) has been derived by accounting only for the diffusion related to viscous sliding. The incorporation of geometric coupling in these calculations warrant the use of an effective D_m which will take into account diffusivity both by viscous sliding and dislocation climb. Additionally, with decreasing grain size the value of GB diffusivity increases [50] thereby reducing r_2 further below the above estimate. Taking all this into consideration, we restrict ourselves to choosing $r_2 = 500$ for our numerical simulations.

3 Results

Let $\tilde{\boldsymbol{x}}$ and $\tilde{t}$ be the non-dimensional position vector and time such that

$$\tilde{\boldsymbol{x}} = \frac{\boldsymbol{x}}{R_0} \text{ and } \tilde{t} = \frac{t}{t_0}, \tag{3.1}$$

where R_0 is a characteristic length and t_0 is a characteristic time. We take R_0 to be a representative length of the initial shape of the embedded grain and t_0 as the time taken for a circular GB with radius R_0, constant GB energy γ_0, and constant mobility M_0 to shrink to a point under curvature driven normal motion. Hence, $t_0 = R_0^2/2\gamma_0 M_0$ [6]. We substitute $\boldsymbol{x}$ and t from (3.1) into (2.9) and (2.10) to obtain the non-dimensionalized kinetic relations involving non-dimensional kinetic parameters r_1 and r_2 and non-dimensional constitutive functions $\tilde{M}$, $\tilde{S}$, and β. The kinetic relations also include the following non-dimensionalized quantities: stress $\tilde{\tau} = R_0\tau/\gamma_0$, bulk stored energy $\tilde{\Psi}^{\pm} = R_0\Psi^{\pm}/\gamma_0$,

and the regularization parameter for the GB energy $\tilde{\delta}_r = \delta_r R_0^2/\gamma_0$. All the non-dimensionalized quantities are distinguished with a superposed tilde.

In this section we use the level set method to solve the coupled system of kinetic relations. The coupled motion is studied first with isotropic GB energy and isotropic kinetic coefficients and then with their anisotropic extensions. We assume throughout that there is no stored energy and stress in the grains. We begin by discussing the essential details of the level set method and the associated numerical schemes. Further details, with several illustrative examples, have been provided in the supplementary document.

3.1 Level set method

In the level set method the isolated GB is considered as the zero level curve of a function $\psi(\boldsymbol{x}, t)$, as shown in Figure 1, where we initialize ψ as a signed distance function (SDF) such that it is negative outside and positive inside of ω^+ (cf. Ch. 2 of [51]). For a given V, ψ is updated with respect to time in the entire domain ω using the Hamilton-Jacobi equation (cf. Ch. 3 of [51])

$$\frac{\partial \psi}{\partial \tilde{t}} + \tilde{V}\,||\nabla \psi|| = 0. \tag{3.2}$$

The updated location of $\psi = 0$ gives the new position of the GB. A computationally less expensive local level set scheme has been proposed by Peng at el. [52], in which ψ, instead of the entire computational domain, is updated only in a small domain in the neighborhood of the zero level curve using the following modified Hamilton-Jacobi equation

$$\frac{\partial \psi}{\partial \tilde{t}} + c(\psi)\tilde{V}_{\text{ext}}||\nabla \psi|| = 0. \tag{3.3}$$

Here $c(\psi)$ is a cut-off function which ensures that ψ is updated only in a narrow region surrounding $\psi = 0$, and $\tilde{V}_{\text{ext}}$ is the (non-dimensional) extended normal velocity (computed using (3.4)). An expression for the cut-off function is provided in the accompanying supplementary document.

We compute extension q_{ext} (non-dimensional) of a given field q by solving the hyperbolic equation [52]

$$\frac{\partial q}{\partial \tilde{t}} + (\operatorname{sign} q)(\boldsymbol{n} \cdot \nabla q) = 0, \tag{3.4}$$

the steady state solution of which, denoted by q_{ext}, satisfies $q_{\text{ext}} = q$ on C and remains constant in the direction of the normal to C.

The updated ψ, obtained by solving (3.3), generally does not remain a SDF [52]. This is resolved by reinitializing ψ to a SDF by solving (locally) [52]

$$\frac{\partial d}{\partial \tilde{t}} + (\operatorname{sign} d_i)(||\nabla d|| - 1) = 0, \tag{3.5}$$

such that $d_i = d(\tilde{\boldsymbol{x}}, 0) = \psi(\tilde{\boldsymbol{x}}, \tilde{t})$. Following Peng et al. [52], we consider

$$\operatorname{sign} d = \frac{d}{\sqrt{d^2 + (||\nabla d||h)^2}}, \tag{3.6}$$

where we have discretized the square domain ω with uniform square grids with mesh size $\tilde{h}$. Let (x_i, y_j) be the $(i,j)_{th}$ node in the 2D lattice grid. At time step t_n and at the $(i,j)_{th}$ grid point, denote the level set function by $\psi_{i,j}$.

We discretize (3.3) using the method of lines. Its semi-discrete form is given by

$$\frac{d\psi_{i,j}}{d\tilde{t}} = L(\tilde{\boldsymbol{x}}, \psi^{\pm}_{\tilde{x}\,i,j}, \psi^{\pm}_{\tilde{y}\,i,j}, \tilde{\kappa}_{i,j}, \boldsymbol{n}_{i,j}, \tilde{\dot{\theta}}), \tag{3.7}$$

where $L = -c\tilde{V}_{\text{ext}}||\nabla\psi||$ and its discretized form is given by

$$L_{i,j} = -\max((c\tilde{V}_{\text{ext}})_{i,j}, 0)||\nabla^{+}\psi||_{i,j} - \min((cV_{\text{ext}})_{i,j}, 0)||\nabla^{-}\psi||_{i,j}, \text{ where} \tag{3.8}$$

$$||\nabla^{\pm}\psi||_{i,j} = [\max(\psi^{\mp}_{x\,i,j}, 0)^2 + \min(\psi^{\pm}_{x\,i,j}, 0)^2 + \max(\psi^{\mp}_{y\,i,j}, 0)^2 + \min(\psi^{\pm}_{y\,i,j}, 0)^2]^{1/2}.$$

Here $\psi^{\mp}_{x\,,i,j}$ and $\psi^{\mp}_{y\,,i,j}$ have been calculated using the fifth order weighted essentially non-oscillatory (WENO) scheme [53]. The time integration of (3.8) has been performed using the third order total variation diminishing (TVD) Runge-Kutta scheme [52]. The reinitialization equation given by (3.5) has also been solved using the same scheme. However first order upwind scheme in space and forward Euler time integration scheme are found sufficient for solving (3.4) [52]. Since we have used the explicit method for time integration of (3.3)-(3.5), the time step chosen must satisfy the Courant-Friedreichs-Lewy (CFL) condition, given by (cf. Ch. 3 of [51])

$$\text{time step} \leq \frac{\tilde{h}}{\max|\text{velocity}|}, \tag{3.9}$$

for maintaining stability, where the 'velocity' is referred to $\tilde{V}_{\text{ext}}$, $\operatorname{sign} q$, and $\operatorname{sign} d_i$, respectively, in (3.3)-(3.5). When the computations are done with isotropic GB energy and the isotropic kinetic coefficients, the time step (non-dimensional) has been taken as $\Delta\tilde{t} = 10^{-4}$ (for (3.3)) so as to satisfy the CFL condition. However, if the GB energy is anisotropic, then we take $\Delta\tilde{t} = 0.5\tilde{h}^4$ [30, 54]. For integrating (3.4) and (3.5), we have taken the time step as $0.6\tilde{h}$, which clearly satisfies the respective CFL conditions.

To compute the boundary integrals in (2.10) of the form $\oint_C f\, d\tilde{s}$, we first replace them by the following integral over the entire domain (cf. Ch. 1 of [51])

$$\int_{\omega} f(\tilde{\boldsymbol{x}})\, \delta(\psi(\tilde{\boldsymbol{x}}))||\nabla\psi||\, d\tilde{a}, \tag{3.10}$$

where $\delta(\psi(\tilde{\boldsymbol{x}}))$ is the Dirac delta function, and then choose the first order accurate expressions for the delta function from [55] for numerical evaluation.

Summary of the computational algorithm

(i) Initialize ψ and θ: Initialize $\psi_i = \psi(\tilde{\boldsymbol{x}}, 0)$ as a signed distance function (SDF). If ψ_i is not an SDF, reinitialize it to convert to an SDF in the domain of computation. Also initialize θ.

(ii) Construct computational tubes: Construct two computational tubes T_1 and T_2 surrounding the zero level set such that $|\psi_i| \leq c_1$ in T_1 and $|\psi_i| \leq c_2$ in T_2. We have taken $c_1 = 2\tilde{h}$ and $c_2 = 4\tilde{h}$, where $\tilde{h}$ is the mesh size. We also construct a third tube $T_3 = \{\tilde{\boldsymbol{x}} : \psi_i(\tilde{\boldsymbol{x}} + \boldsymbol{\delta}) < c_2, \text{ for } |\boldsymbol{\delta}| < \tilde{h}\}$ [52]. Tube T_3 contains T_2 in addition to the grid points which are just adjacent to T_2.

(iii) Constitutive relations: Compute $\tilde{\gamma}$, $\tilde{M}$, $\tilde{S}$, and β as functions of θ and ϕ.

(iv) Computation of $\tilde{\kappa}$ and its surface Laplacian: Compute $\tilde{\kappa}$ and its surface Laplacian first inside T_1, and then extend it to $T_2 \backslash T_1$. For solving the extension equation (3.3) we have taken $\Delta\tilde{t} = 0.6\tilde{h}$, and used six iterations so that the extended quantities in $T_2 \backslash T_1$ reach their steady state values.

(v) Computation of the kinetic relations: Compute $\tilde{\dot{\theta}}$ and $\tilde{V}$ inside T_1 and then extend them to $T_2 \backslash T_1$.

(vi) Updating of ψ and θ: Integrate the modified Hamilton-Jacobi equation given by (3.3) inside T_2, along with updating θ. For computations with isotropic GB energy and isotropic kinetic coefficients, we have taken $\Delta\tilde{t} = 10^{-4}$, whereas for those with anisotropic energy, we have considered $\Delta\tilde{t} = 0.5\tilde{h}^4$.

(vii) Reinitialization: Reinitialize ψ (which was computed in step (vi)) inside region T_3 using the reinitialization equation (3.5). We have iterated the reinitialization equation once after every time update of ψ in Step (vi) by taking $\Delta\tilde{t} = 0.6\tilde{h}$.

(viii) Once the new ψ (which is a SDF) is obtained, go to step (i) and repeat the calculation.

3.2 Isotropic energy and isotropic kinetic coefficients

In their atomistic simulations Cahn et al. [5] observe viscous sliding of the grains along the GB to be the dominant mechanism for grain rotation at high temperatures near the melting point, and the geometric coupling factor β to govern the rotation at lower temperatures. It is therefore important to compare the dynamics of coupled motion dominated by different kinetic coefficients and observe their individual and collective role in influencing the overall GB motion. Depending on the temperature of the specimen and the geometry of the boundary, some or all of the coefficients may contribute to the resulting dynamics. The dependence of the coefficients on the misorientation angle is also of crucial importance. The purpose of this section is to investigate the relative role of these coefficients during GB motion with isotropic GB energy. The governing equations can be obtained by substituting $\partial^2\tilde{\gamma}_c/\partial\phi^2 = 0$ and $\tilde{\delta}_r = 0$ in the non-dimensionalized form of (2.9) and (2.10) combined with the isotropic $\tilde{M}, \tilde{S}$, and β. We study the effect of various kinetic coefficients on the shape evolution of circular, near-circular, and non-circular GBs. We also verify our simulation results with the analytical solutions obtained for circular and near-circular GBs. Additionally, our results include studying the effect of misorientation dependence of coefficients on GB motion, the

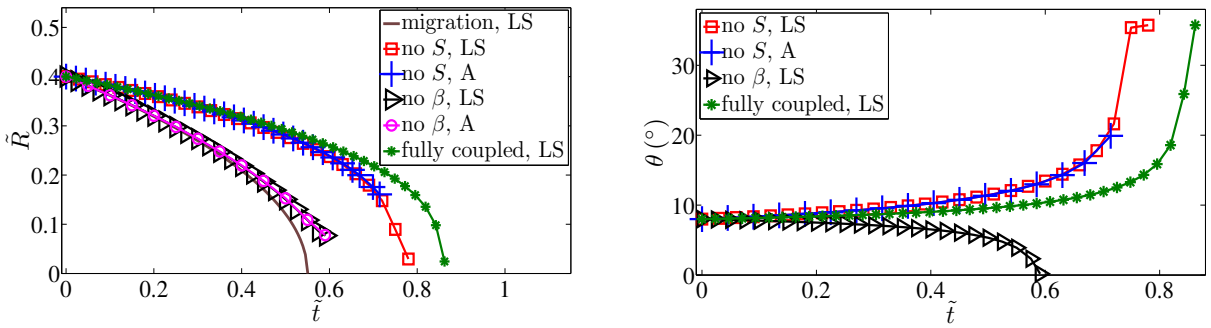

(a) (b)

Figure 6: Evolution of (a) GB radius and (b) misorientation for circular GB with $\tilde{R}_i = 0.4$ and $\theta_i = 8°$. We have taken $\tilde{M} = 1$, and $r_1 = 0.01$, $\tilde{S} = 1$ whenever sliding is present. In the legends, 'LS' and 'A' stand for level set results and analytical results, respectively.

role of viscous sliding in GB dynamics, the effect of external stress, and finding fixed points in the evolution of misorientation angle.

For all our level set computations with isotropic energy and isotropic kinetic coefficients, we have discretized a square domain $[-1, 1] \times [-1, 1]$ with $N = 100$ grid points at equal intervals along each of $\boldsymbol{e}_1$ and $\boldsymbol{e}_2$ directions. We have taken $\Delta\tilde{t} = 10^{-4}$. The external stress field is taken to be zero in all our simulations except in Subsection 3.2.4.

3.2.1 Coupled motion of a circular GB

The kinetic relations can be solved analytically under various simplifying assumptions for a circular GB. The reduced kinetic relations are derived from (A.27) and (A.28). We compare the following four cases indicating the analytical result whenever possible, cf. [6, 7].

(i) (Both viscous sliding and geometric coupling absent) The kinetic relations reduce to $\tilde{V} = \tilde{M}\tilde{\gamma}_c\tilde{\kappa}/2$ and $\dot{\theta} = 0$, which can be solved to obtain

$$\tilde{R}(\tilde{t}) = \sqrt{\tilde{R_i}^2 - \tilde{M}\tilde{\gamma}_c\tilde{t}} \text{ and } \theta = \theta_i, \tag{3.11}$$

where $\tilde{R}_i$ and θ_i denote the initial GB radius and the initial misorientation, respectively.

(ii) (Viscous sliding absent) The kinetic relations simplify to

$$\tilde{V} = -\frac{1}{\beta}(\tilde{\boldsymbol{x}} \cdot \tilde{\boldsymbol{n}})\dot{\theta} \text{ and } \dot{\theta} = \frac{1}{2\tilde{R}^2}\tilde{M}\beta\left(\tilde{\gamma}_c - \beta\frac{\partial\tilde{\gamma}_c}{\partial\theta}\right). \tag{3.12}$$

This situation is typical of low angle boundary dynamics at temperatures much below the melting point. To this end, we take $\tilde{\gamma}_c$ as the first expression in (2.11) (with $\phi = 0$), and $\beta = \theta$ following (2.19). The above equations can be solved, using $\tilde{\boldsymbol{x}} \cdot \tilde{\boldsymbol{n}} = -\tilde{R}$ and $\tilde{V} = -\dot{\tilde{R}}$, to obtain $\tilde{R}\theta =$ constant.

For a given initial radius $\tilde{R}_i$ and misorientation θ_i, the constant is equal to $\tilde{R}_i\,\theta_i$. Finally, substituting $\tilde{R}\,\theta = \tilde{R}_i\,\theta_i$ into (3.12) and treating $\tilde{M}$ as a constant, we obtain

$$\tilde{R}(\tilde{t}) = \tilde{R}_i\theta_i\left(\frac{1}{\theta_i^3} - \frac{3\tilde{M}\tilde{t}}{2\tilde{R}_i^2\theta_i^2}\right)^{1/3} \text{ and } \theta(\tilde{t}) = \left(\frac{1}{\theta_i^3} - \frac{3\tilde{M}\tilde{t}}{2\tilde{R}_i^2\theta_i^2}\right)^{-1/3}. \tag{3.13}$$

(iii) (Geometric coupling absent) This case is relevant when the tangential motion of the grains is predominantly due to the viscous sliding, for instance with temperatures close to the melting point [5]. The non-dimensional kinetic relations can be obtained as

$$\tilde{V} = \frac{1}{2}\tilde{M}\tilde{\gamma}_c\tilde{\kappa} \text{ and } \dot{\theta} = -\frac{r_1\tilde{S}}{2\tilde{R}^2}\frac{\partial\tilde{\gamma}_c}{\partial\theta}. \tag{3.14}$$

For constant $\tilde{M}$ and $\tilde{S}$, these equations can be solved simultaneously to get the following relation between $\tilde{R}$ and θ:

$$\tilde{R}(\theta) = \tilde{R}_i\exp\left(\frac{\tilde{M}}{r_1\tilde{S}}\left\{\frac{(\theta^2-\theta_i^2)}{2} - e^{2(A_c-1)}[E(1,u_i)-E(1,u)]\right\}\right), \tag{3.15}$$

where $u = 2(A_c - 1 - \ln\theta)$, $u_i = 2(A_c - 1 - \ln\theta_i)$, and $E(n,x) = \int_x^\infty \frac{e^{-u}}{x^{1-n}u^n}du$ (the exponential integral). For plotting the analytical solution in Fig. 6(a) we have used θ from the numerical simulations.

(iv) (Fully coupled) The governing equations, deducible directly from (2.9) and (2.10) by assuming a circular GB, are given by

$$\tilde{V} = \frac{r_1\tilde{M}\tilde{S}}{r_1\tilde{S}+\tilde{M}\beta^2}\frac{\tilde{\gamma}_c}{\tilde{R}} + \frac{\tilde{M}\beta}{r_1\tilde{S}+\tilde{M}\beta^2}\tilde{R}\dot{\theta} \text{ and } \dot{\theta} = \frac{\tilde{M}\beta\tilde{\gamma}_c - (r_1\tilde{S}+\tilde{M}\beta^2)(\partial\tilde{\gamma}_c/\partial\theta)}{\tilde{R}^2}, \tag{3.16}$$

which cannot be solved analytically even for constant $\tilde{M}$ and $\tilde{S}$. The above pair of governing equations, as well as the corresponding relations in all the preceding cases, indicate that the shrinkage rate of the circular GB is inversely proportion to its radius while the rate of misorientation change is inversely proportional to the square of the radius.

The analytical solutions derived in (3.11), (3.13), and (3.15) confirm well with our level set simulation results, see Figures 6(a) and 6(b). The same figures are also used to compare the four cases with respect to area and misorientation evolution. The results clearly demonstrate the distinctive role of various kinetic parameters even in this simplified illustration. For instance, we note that the inner grain, in all the cases, shrinks at a slower rate than it does during a purely normal motion. In fact, for the fully coupled case, both the shrinkage rate as well as the misorientation evolution is the slowest. On the other hand, the absence of coupling factor yields very distinctive results. Not only the shrinkage rate is much faster, regardless of viscous sliding, it is only in this situation that the misorientation is found to be non-increasing with time. With respect to the latter observation we would like to add that, while in cases with β present the misorientation angles evolve toward a fixed point around θ_β, in the situation with β absent but sliding allowed it evolves to 0°. The nature of fixed points in the evolution of θ is even otherwise very sensitive to the choice of constitutive assumptions and initial conditions, see Subsection 3.2.6 for further analysis.

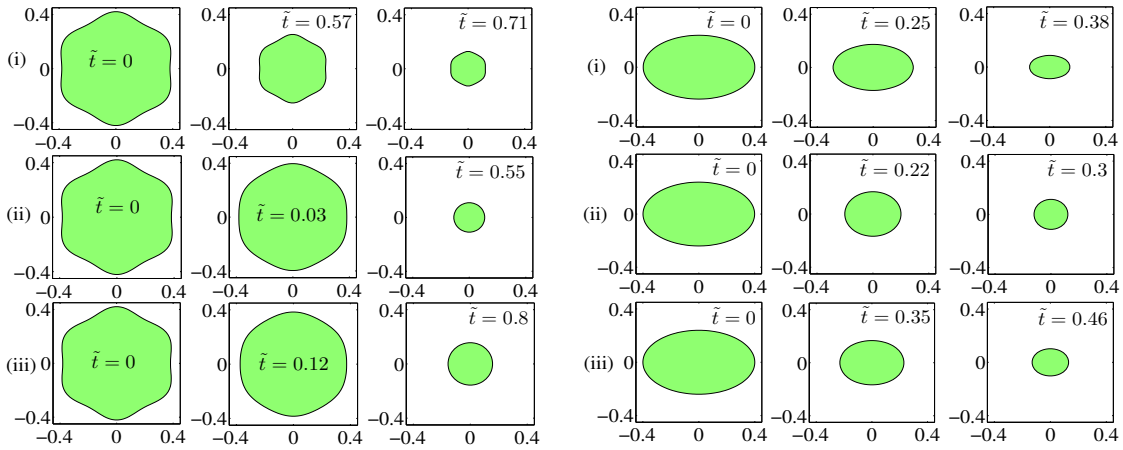

(a) (b)

Figure 7: (a) Evolution of an initially near-circular GB with $m = 6$, $\tilde{R}_{mi} = 0.4$, and $\epsilon = 0.05$. (b) Evolution for an initially elliptic GB with the semi-major axis of length 0.4 and the semi-minor axis of length 0.24. The three cases shown here are: (i) viscous sliding absent, (ii) geometric coupling absent with $r_1 = 0.01$ and $\tilde{S} = 1$, and (iii) fully coupled with $r_1 = 0.01$ and $\tilde{S} = 1$. For all of these simulations, $\tilde{M} = 1$ and $\theta_i = 8^\circ$.

3.2.2 Coupled motion of a near-circular GB

Following Taylor and Cahn [7], we call a GB near-circular if its shape is represented by

$$\tilde{R}(\zeta, \tilde{t}) = \tilde{R}_m(\tilde{t}) + \epsilon \tilde{R}_\epsilon(\tilde{t}) \cos(m\zeta), \tag{3.17}$$

where $\tilde{R}_m(\tilde{t})$ is the mean circular radius of the GB, $\epsilon \ll 1$ is a constant parameter, $\epsilon\tilde{R}_\epsilon(t)$ is the amplitude of the deviation from the mean radius, ζ is the angle made by the radial vector with $\boldsymbol{e}_1$-axis, and m is an integer which governs the shape of the perturbation. We restrict the latter such that $m \geq 2$, since $m = 0$ corresponds to a circle and $m = 1$ to an offset circle. We illustrate the evolution of a near-circular GB with $m = 6$ in Figure 7(a) for various simplifying assumptions. We note, in particular, that allowing for viscous sliding will eventually change the shape of an initially near-circular grain to a circle, but its absence will restrict the grain to shrink in a self-similar manner. The inclusion of coupling factor, on the other hand, always slows down the shrinkage rate of the inner grain. These conclusions are corroborated in the following analysis.

(i) (Viscous sliding absent) The kinetic relation (A.27) is reduced by $\dot{\tilde{R}} = -\tilde{R}\dot{\theta}/\beta$. This can be integrated to obtain

$$\frac{\tilde{R}(\zeta_1, \tilde{t})}{\tilde{R}(\zeta_2, \tilde{t})} = \frac{\tilde{R}(\zeta_1, 0)}{\tilde{R}(\zeta_2, 0)}. \tag{3.18}$$

According to the above solution, the shape of the GB at any time $\tilde{t}$ remains self-similar to the initial shape, cf. [7]. Interestingly, the above analysis remains valid irrespective of grain shape and

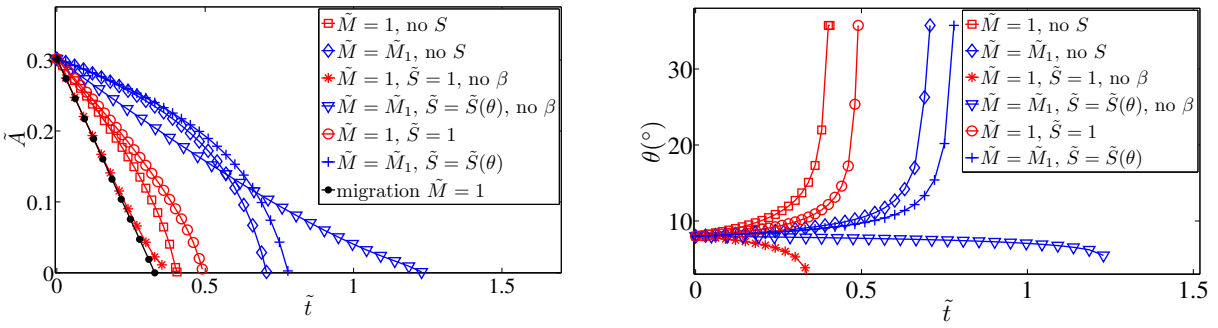

(a) (b)

Figure 8: (a) Area and (b) misorientation evolutions of the elliptic GB under coupled motion with $\theta_i = 8^\circ$ and $r_1 = 0.01$.

constitutive assumptions, i.e. it remains valid even for anisotropic GB energy and kinetic coefficients, as long as β remains isotropic. It should be noted that a self-similar shape is obtained in the absence of viscous sliding only when geometric coupling is present in the kinetic relations. Whenever coupling is absent, regardless of viscous sliding, the normal and the tangential motion of the GB are decoupled and the shape evolution is always driven by mean curvature. In a coupled motion, however, shape smoothening driven by curvature can take place only when sliding is allowed.

(ii) (Geometric coupling absent) We can expand the kinetic relation (2.9), after reducing it for the present case, in power series of ϵ to get

$$\dot{\tilde{R}}_m + \epsilon\dot{\tilde{R}}_\epsilon \cos(m\zeta) = -\frac{\tilde{M}\tilde{\gamma}_c}{2\tilde{R}_m}\left(1 + \epsilon(m^2-1)\cos(m\zeta)\frac{\tilde{R}_\epsilon}{\tilde{R}_m}\right) + \mathcal{O}(\epsilon^2). \tag{3.19}$$

Equating the leading order terms on both sides of the equation we get the governing equation for $\tilde{R}_m$, which is of the same form as $(3.14)_1$. The $\mathcal{O}(\epsilon)$ terms, on the other hand, yield $\dot{\tilde{R}}_\epsilon = -(m^2-1)\tilde{M}\tilde{\gamma}_c\tilde{R}_\epsilon/2\tilde{R}_m^2$, which on integration gives

$$\tilde{R}_\epsilon(\tilde{t}) = \tilde{R}_{\epsilon i}\exp\left(-\int_0^{\tilde{t}} \frac{\tilde{M}\tilde{\gamma}_c(m^2-1)}{2\tilde{R}_m^2}d\tilde{t}\right), \tag{3.20}$$

where $\tilde{R}_{\epsilon i} = \tilde{R}_\epsilon(\zeta, 0)$. For $m \geq 2$, the integrand in (3.20) is always a positive function of $\tilde{t}$, making the resulting integral an increasing function of $\tilde{t}$. Thus $\tilde{R}_\epsilon$ goes to zero with time and the near-circular shape tends toward a circular form.

3.2.3 Coupled motion of a non-circular GB

Moving on to a more general case, we now investigate the coupled motion of a non-circular GB with isotropic GB energy and isotropic kinetic coefficients from Subsection 2.3. For illustration we consider an initially elliptic GB with aspect ratio 5/3. Figure 7(b) demonstrates that the shape

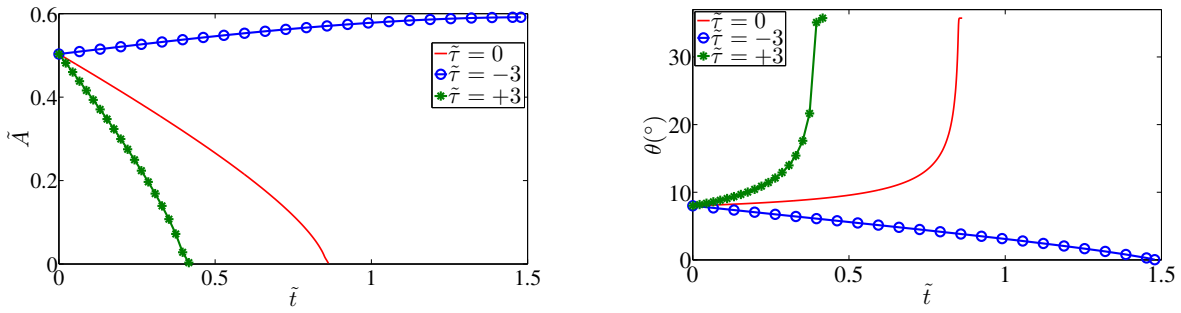

(a) (b)

Figure 9: Evolution of the (a) area enclosed by a circular GB, and (b) the misorientation angle with $\tilde{\tau} = 0$, $\tilde{\tau} = -3$, and $\tilde{\tau} = 3$. We have taken $r_1 = 0.01$, $\tilde{M} = 1$, and $\tilde{S} = 1$.

evolution behavior of the elliptic GB is qualitatively identical to the near-circular GB. The GB always shrinks to a circular shape in the presence of viscous sliding but to a self-similar shape in its absence. Moreover, the shrinkage is faster if the coupling factor is ignored. In Figures 8(a) and 8(b) we have compared the evolution of both the area enclosed by the GB and the misorientation angle under various assumptions on the kinetic coefficients. We find that the misorientation dependence of the mobility, as well as of the sliding coefficient, yields significant influence on the GB dynamics. These coefficients were taken to be unity, whenever present, in all of the previous simulations. The misorientation dependence slows down the shrinkage rate and, unlike what was observed earlier, the rate is slowest when both $\tilde{M}$ and $\tilde{S}$ depend on θ in addition to β being absent (the fully coupled case is faster). The shrinkage rate remains fastest for a purely normal motion. The rate of misorientation evolution is also considerably slower when the coefficients depend on θ. The misorientation angle increases to a fixed point, close to θ_β, for all the cases which incorporate geometric coupling. The reason for θ to increase rapidly towards the end, before reaching the fixed point, can be explained by noticing the almost shrunk size of the inner grain at these time instances. The absence of the coupling factor however drives the misorientation towards zero. We provide a more detailed analysis of the misorientation dynamics in Subsection 3.2.6. Finally we note that, although the shape of the GB does not change without viscous sliding, the inner grain continues to rotate due to the geometric coupling.

3.2.4 Effect of external stress

Assume the bicrystal arrangement to be under the influence of a uniform shear stress $\tilde{\tau}$. The kinetic relations (2.9) and (2.10) incorporate the effect of stress through f_s, see $(A.21)_2$. To illustrate the significance of stress we look at the area and the misorientation evolution of a circular GB with and without the external stress. We find that, for $\tilde{\tau}$ below a critical value, the direction of the evolution

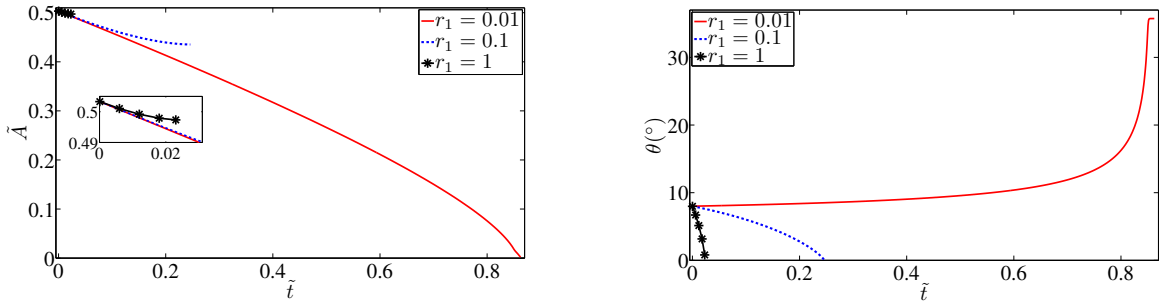

(a) (b)

Figure 10: Evolution of (a) the radius and (b) the misorientation of a circular GB for varying r_1, where $\tilde{M} = 1$ and $\tilde{S} = 1$

is reversed. For $r_1 = 0.01$ and a circular GB the critical stress is around -3. We have compared the evolution of area and misorientation at $\tilde{\tau} = \pm 3$ with that at zero stress in Figure 9. For a positive shear stress the grain continues to shrink but at an increased rate. Likewise the the change of misorientation angle becomes more rapid as the stress is increased from zero level. We note that the considered value of stress is insufficient to initiate plastic deformation of the grains. Indeed, for $\tilde{\tau} = 3$, $\gamma_0 \sim 1\text{N/m}$, and $R_0 \sim 20 \times 10^{-9}\text{m}$ we get $\tau = \gamma_0 \tilde{\tau}/R_0 \sim 240\text{MPa}$. For nanocrystalline grains the yield stress is however of the order of several tens of GPa [8].

3.2.5 Role of sliding

The significance of viscous sliding along a GB increases as the operating temperatures tend towards the melting point. It can be negligible for lower temperatures. We have already seen that the presence of viscous sliding will always turn any arbitrary GB circular, while its absence will keep it self-similar. In the present discussion we would like to investigate further the role of sliding in the dynamic process. To do so, we study the area and the misorientation evolution of a circular GB for different values of r_1. The results are given in Figures 10(a) and 10(b). We note that with an increasing r_1, which is equivalent to an increasing sliding coefficient, the bicrystal turns into a single grain much faster, either by shrinking of the inner grain or by diminishing of the misorientation angle through the relative rotation. While looking at the plots, it should be remembered that the evolution ceases as soon as the inner grain is completely shrunk or the misorientation angle has become zero.

3.2.6 Misorientation evolution as a dynamical system

We have observed, in several instances above, the misorientation angle to evolve to a fixed value thereby freezing any further relative rotation of the grains. The nature of misorientation evolution and the associated fixed points was found to be highly sensitive to the choice of constitutive as-

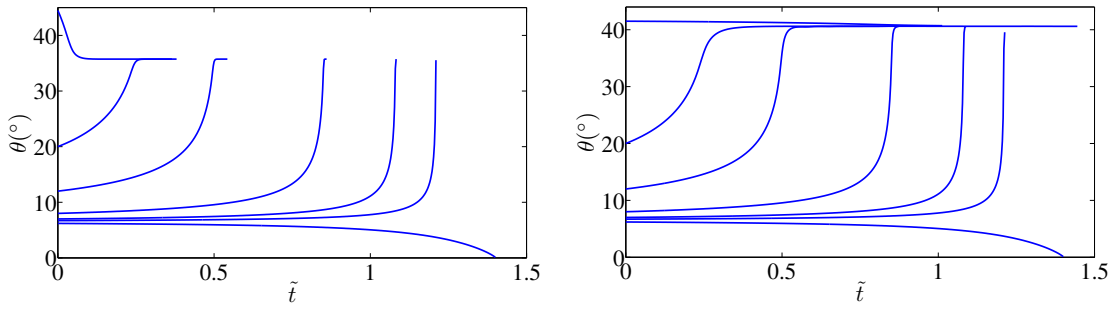

(a) (b)

Figure 11: Flow diagram for θ with (a) β as given in (2.19), and when (b) $\beta = 2\tan(\theta/2)$ for all θ. Both the diagrams show two stable fixed points and one unstable fixed point. We have used $\tilde{R}_i = 0.4$, $r_1 = 0.01$, $\tilde{M} = 1$, $\tilde{S} = 1$.

sumptions as well as the initial conditions such as shape, etc. It should be mentioned that the GB continues to migrate even when the misorientation has reached a fixed point, unless the point corresponds to 0°. The purpose of this subsection is to study misorientation evolution as a dynamical system and analyze the nature of its fixed points. For illustration purposes we restrict our attention to circular GBs with constant coefficients for mobility and viscous sliding. The fixed points for the considered system can be obtained as the zeros of the right hand side of $(3.16)_2$. In Figure 11 we show the flow diagram for the misorientation angle for a circular GB with the mentioned parameters. We investigate the effect of the sharp transition in the variation of β given in (2.19). In Figure 11(a) we consider this β with the general form of isotropic GB energy to observe three fixed points in the range $0^\circ \leq \theta \leq 45^\circ$. The two stable points occur at 0° and at an angle close to θ_β. The unstable fixed point is located around 6.5°. On the other hand, if we ignore the transition in β, and take it to be $2\tan(\theta/2)$ for all θ, then the second stable fixed point moves to a value close to $\theta = 40.6^\circ$. Whereas in the former case the transition in β dominates over the effect of cusp in γ_c in determining the fixed point [14], it is the absence of change of mode in β that is responsible for the deviation of the fixed point away from the cusp angle in the latter scenario. The MD simulation results in [16] predict a stable fixed point in a very small neighborhood of the cusp angle $\theta_c = 36^\circ$.

3.3 Anisotropic GB energy and anisotropic kinetic coefficients

We now turn our attention towards the coupled GB motion allowing for anisotropy in both the GB energy and the kinetic coefficients. The form of the considered anisotropy has been already specified in Subsection 2.3. The role of anisotropic GB energy in the determination of an equilibrium shape (Wulff shape) of a GB, as well as in studying its migration, is well understood (cf. §5.6 of [2] and the references therein). The anisotropy is known to yield faceted GBs such that, under capillarity

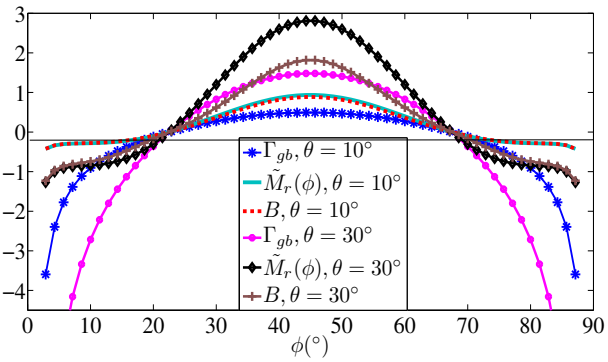

Figure 12: Plot for the GB stiffness $\Gamma_{gb} = \tilde{\gamma}_c + \partial^2\tilde{\gamma}_c/\partial\phi^2$, reduced mobility $\tilde{M}_r(\phi) = \tilde{M}_2(\phi)\Gamma_{gb}$, and the term $B = r_1\tilde{M}_2\tilde{S}/(r_1\tilde{S} + \tilde{M}_2\beta^2)\Gamma_{gb}$ at $\theta = 10°$ and $30°$. We have taken $r_1 = 1$, $\tilde{S} = 1$, and β to be anisotropic.

forces, any initial GB shape will turn into a polygon. The purpose of this section is to study the influence of kinetic coefficients and their anisotropy on the shape and misorientation evolution of a GB with anisotropic energy. We also provide a detailed comparative study to bring out the effect of anisotropy in the mobility coefficient and the geometric coupling factor.

To appreciate the challenge in implementing a numerical procedure for anisotropic energies assume for now that only migration (with constant mobility) is allowed. The GB stiffness $\Gamma_{gb} = \gamma_c + \partial^2\gamma_c/\partial\phi^2$ for anisotropic energies, such as those given in (2.11), is negative over certain values of ϕ. The region spanned by these values constitute the GB spinodals [29]. Figure 12 shows the GB stiffness (red lines) in the inclination range $0° < \phi < 90°$ for different misorientation angles. We notice that for any misorientation angle the GB stiffness changes sign at two fixed inclinations $\phi = 22.5°$ and $67.5°$. This is due to the decoupled dependence of the stiffness on θ and ϕ for the energy given by (2.11). For GB spinodals, the governing equation for normal velocity (2.9) becomes backward parabolic and hence ill posed [30]. It therefore becomes necessary to regularize the GB energy using a curvature dependent energy, see (A.14). A quadratic regularizing energy introduces a surface Laplacian of the mean curvature in (2.9) and (2.10). This higher order derivative requires a time step $\Delta\tilde{t} \sim \tilde{h}^4$, where $\tilde{h}$ is the grid size, when (2.9) is integrated using the explicit time integration scheme [54]. Therefore higher accuracy in the solution (lower $\tilde{h}$) has to be balanced with increased simulation time.

The computational domain has been taken to be a square with coordinates $[-1, 1] \times [-1, 1]$ with $N = 45$ grid points in each direction. The time step is taken as $\Delta\tilde{t} = 0.5\tilde{h}^4$ to avoid instability in the numerical calculations. In special cases, e.g. when the sliding is absent and the surface Laplacian term disappears from (2.9), a larger time step $\Delta\tilde{t} = 10^{-4}$ has been used.

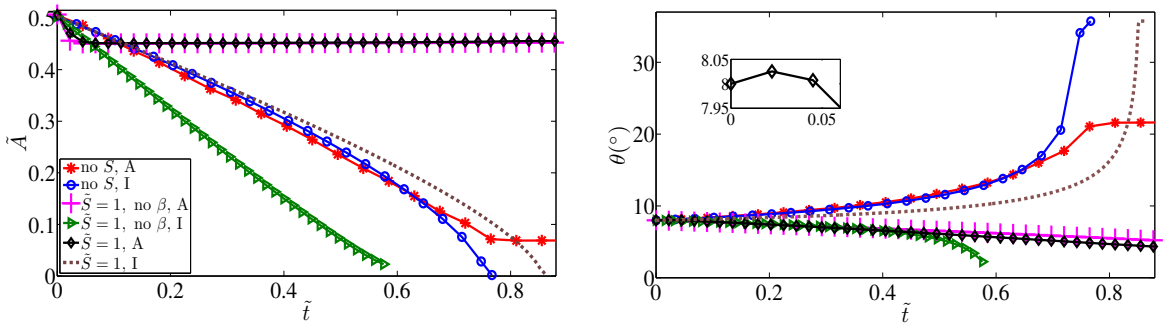

(a) (b)

Figure 13: (a) Area and (b) misorientation evolution when the GB energy is isotropic (denoted by I in the legend) and anisotropic (denoted by A in the legend). We have used $r_1 = 0.01$, $\tilde{M} = 1$, and $\tilde{S} = 1$. The GB has been initially taken to be circular with $\tilde{R}_i = 0.4$ and $\theta_i = 8^\circ$. The legend is shared between both the figures.

3.3.1 Effect of anisotropic energy

We start by looking at the coupled motion with anisotropic GB energy while keeping all the kinetic coefficients either constant or isotropic. In Figures 13(a) and 13(b) we have compared the evolution of the inner grain area and the misorientation under isotropic and anisotropic energies for various choices of kinetic parameters. These choices as well as the initial conditions are kept identical to those taken earlier in Figure 6. When viscous sliding is absent, the evolutions are initially similar for both isotropic and anisotropic GB energy. However, after a while, the misorientation for the latter case stops evolving due to a negligible contribution from the integral involving the torque term $\partial\tilde{\gamma}_c/\partial\theta$. Moreover, the shape of the GB remains self-similar with area ceasing to evolve once the rotation stops.

The dynamics is completely different when viscous sliding is active. First we consider the case of zero geometric coupling. The non-dimensionalized form of (2.9) and (2.10) are then given by

$$\tilde{V} = \frac{1}{2}\tilde{M}\tilde{f}_{\text{curv}} \text{ and } \dot{\theta} = \frac{-\oint_C (\partial\tilde{\gamma}_c/\partial\theta)ds}{\oint_C 2(\tilde{\boldsymbol{x}}\cdot\boldsymbol{n})^2/(r_1\tilde{S})ds - \oint_C r_2\left(\tilde{R}^2 - \overline{\tilde{R}^2}\right)^2 ds}. \tag{3.21}$$

Equation $(3.21)_1$ is of the same form as the well studied kinetic law for GB migration (cf. Ch. 8 of [36]) except for the fact that GB energy, and hence the stiffness, is now varying with misorientation. The GB shapes are expected to evolve towards the local equilibrium (Wulff shapes) corresponding to the instantaneous misorientation angle after a sufficiently long time from $\tilde{t} = 0$. The equilibrium shape reached at large time depends of course on the initial misorientation. This is confirmed from the shape evolutions given in Figures 14(a)(i) and 14(b)(i), where we also note the existence of an unstable fixed point between 22° and 23° in the evolution of θ. Whereas the former initial condition

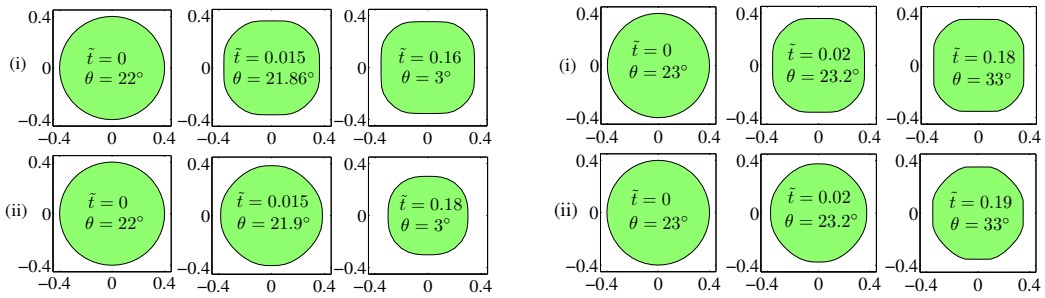

(a) (b)

Figure 14: Evolution of an initially circular GB with (a) $\theta_i = 22°$ and (b) $\theta_i = 23°$ when (i) GB energy is anisotropic and $\tilde{M} = 1$ and (ii) both GB energy and mobility are anisotropic such that $\tilde{M} = \tilde{M}_2(\phi)$. We have taken $r_1 = 1$, $\tilde{S} = 1$, $\tilde{\tau} = 0$, and geometric coupling to be absent.

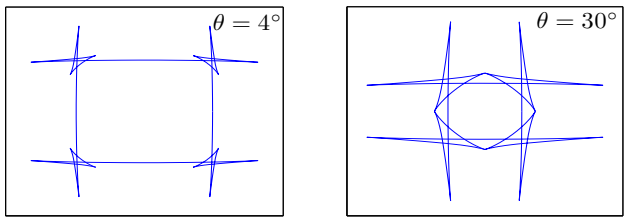

Figure 15: The graphs generated by the Cahn-Hoffman vector $\tilde{\gamma}_c \boldsymbol{n} - \frac{\partial \tilde{\gamma}_c}{\partial \phi} \boldsymbol{t}$ for $\theta = 4°$ and $\theta = 30°$. In plotting these graphs we have smoothened the cusps in the non-differentiable energy.

takes the GB towards a more square like shape, the latter develops it as an octagon. To explain this, we recall that the Wulff shape of a crystal for a given energy has the form of the innermost convex envelope generated by the graph of the Cahn-Hoffman vector (cf. §5.6.4 of [2]). The plots for the Cahn-Hoffman vector corresponding to $\theta = 4°$ and $30°$ are given in Figure 15. The 'ears' in these plots correspond to the spinodals. For $\theta = 4°$ the envelope is square with narrow truncated corners, whereas, at a larger misorientation angle $30°$, the shape develops much wider corners. This is due to the appearance of additional local minimas in the energy plot at higher misorientation angles, see Figure 2(b). Hence, as the misorientation increases, the Wulff shape begins to contain wider and flattened corners leading to an octagonal appearance. The area and the misorientation evolution of an initially circular GB, in the absence of geometric coupling and constant mobility and viscous sliding coefficients, are shown in Figures 13(a) and 13(b). The corresponding shape evolution is shown in Figure 16(i). We observe an almost 10% drop in the area until $\tilde{t} = 0.04$ after which the area evolution becomes negligible; the misorientation however continues to decrease. The former can be explained by noting the appearance of facets in Figure 16(i) as early as $\tilde{t} = 0.02$, which results in diminishing of the weighted curvature in the right hand side of $(3.21)_1$. The evolution

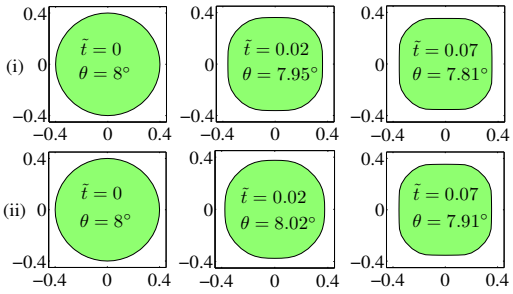

Figure 16: Shape evolutions of an initially circular GB under anisotropic GB energy for (i) no β and (ii) the fully coupled case. We have taken $\tilde{M} = 1$, $\tilde{S} = 1$, and $r_1 = 0.01$.

of the misorientation towards $\theta = 0$ is dominated by the integral involving the torque term in the numerator of $(3.21)_2$.

Next we consider the fully coupled case with isotropic β in addition to constant mobility and viscous sliding coefficients. The area and the misorientation evolution of an initially circular GB, as shown in Figures 13(a) and 13(b), follow trends very similar to the preceding case. The corresponding shape evolution is given in Figure 16(ii). Interestingly, for our choice of initial conditions and material parameters, the misorientation evolution is briefly non-monotonic in the beginning, see inset in Figure 13(b) and Figure 16(ii). This can be explained by recalling (2.10). The first integral in the numerator, which is initially greater than the integral containing the torque term $\partial\tilde{\gamma}/\partial\theta$, become vanishing small as the facets are formed thereby allowing the torque term to dominate. Secondly, the misorientation now approaches zero, unlike with isotropic energy where it increases to a finite value.

The effect of introducing isotropic β on the shape evolution, while keeping other parameters unchanged, can be observed from Figure 16 as well as from Figures 14(a)(i) and 17(i). In Figure 14(a)(i) there is little difference in the shape evolution as well as the eventual direction of the misorientation orientation, although one can notice a small delay in the appearance of facets. In Figure 17(i) however the direction of misorientation evolution is reversed. Keeping β isotropic, the influence of initial conditions on the shape evolution can be seen in Figures 18(a)(i) and 18(b)(i). The shear stress is taken to be a finite value in both of these cases. The misorientation value of around 30° is reached much faster in the former case without any appreciable shape change. That the effect of stress is significant on both the shape and the misorientation evolution can be seen by comparing Figures 17(i) and 18(a)(i).

We would like to mention that, for all the cases considered in Figure 18(a) including the one mentioned above, the rate of misorientation change is extraordinarily large. This is happening because of the two positive terms in the denominator of (2.10) becoming very close to each other. We should recall that our derivation of linear kinetic laws is based on the assumption of slow kinetics and therefore we should exercise caution in interpreting such results.

3.3.2 Effect of anisotropic mobility

We investigate the influence of anisotropic mobility coefficient upon the GB evolution, starting by assuming the geometric coupling to be absent, see Figures 14(a) and 14(b). The governing equations are again reduced to (3.21) but now with $\tilde{M}$ depending additionally on ϕ. We note that, for the given parameters, the unstable fixed point persists between 22° and 23°. There are two noticeable points in each of these two cases. With the introduction of anisotropic mobility the GB shape is more curved, or in other words less faceted, and the inner grain experiences larger shrinkage. Both of these results are in good qualitative agreement with the phase field and the molecular dynamic simulations of Kazaryan et al. [42] and Lobkovsky et al. [44], respectively. To explain this we recall, using $(3.21)_1$, that the shape of the inner grain at large times (the equilibrium shape) is now governed by reduced mobility $\tilde{M}_r(\phi) = \tilde{M}_2(\phi)\Gamma_{gb}$ instead of just GB stiffness, where we have used $\tilde{M} = \tilde{M}_2(\phi)$. We observe from Figure 12 that although the spinodals do not change, owing to the decoupling between θ and ϕ, the reduced mobility for globally stable inclinations (where the GB stiffness is non-negative) is higher than the GB stiffness. This forces the portions on the GB with globally stable inclinations to move by larger distances compared to the case when the mobility is isotropic. As a result the adjacent facetted regions are shrunk making the shapes look more rounder than before. The stiffness difference, and therefore the rounding effect, is larger for higher misorientation angles.

Now we consider the evolution with anisotropic mobility with isotropic coupling factor. The shape evolution is governed by (2.9), where the weighted curvature term tries to flatten out the spinodals from the GB whereas the $\dot{\theta}$ dependent term tries to form a 45° rotated square like shape due to its four-fold symmetry. The first term involves a modified stiffness factor $B = r_1\tilde{M}_2\tilde{S}/(r_1\tilde{S} + \tilde{M}_2\beta^2)\Gamma_{gb}$ which reduces to $\tilde{M}_r$ when β is absent. The values of B remain very close to those of $\tilde{M}_r$ at lower misorientation angles with increasing deviation for higher angles. The influence of incorporating β on shape evolution can be seen by comparing Figures 14(a)(ii) and 17(ii). Most interestingly, the direction of misorientation evolution is itself reversed suggesting that the earlier existence of a fixed point between 22° and 23° is now lost. Hence the shape evolution in the latter case would look very similar for $\theta_i = 23°$, thereby warranting a comparison between Figures 14(b)(ii) and 17(ii). For the parameters considered, the shape evolution in Figure 17(ii) is dominated by the weighted curvature term since the misorientation rates remain low. The situation is reversed if stress is introduced in the problem as discussed next.

The presence of a constant shear stress field manifests itself on the numerator of the misorientation evolution equation (2.10). It can have a significant effect on the shape evolution, as can be seen on comparing Figures 17(ii) and 18(a)(ii). In the latter, the shape is evolved towards a rotated square. Indeed, the introduction of stress greatly increases the misorientation rate forcing the $\dot{\theta}$ dependent term in (2.9) to dominate over the weighted curvature term. The shapes are then governed by kinetic relations of the form $\tilde{V} = \tilde{M}_2(\phi)$ which owing to the four-fold symmetry of anisotropic mobility leads to rotated squares. On the other hand, we see from Figure 18(b) that having a sufficiently large shear

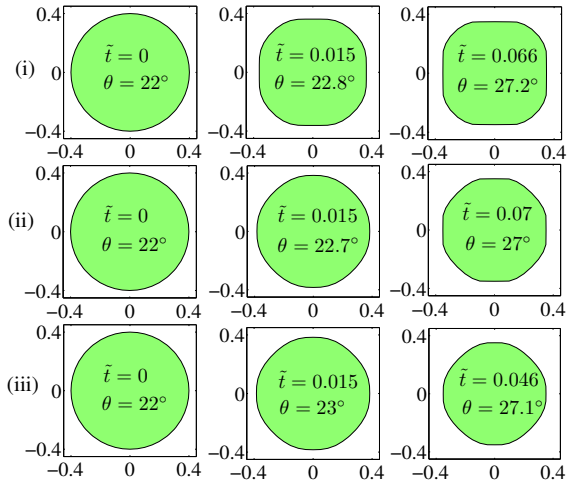

Figure 17: Evolutions of an initial circular GB with $\theta_i = 22°$ when (i) GB energy is anisotropic, $\tilde{M} = 1$, and $\beta = \beta(\theta)$, (ii) GB energy and mobility are anisotropic ($\tilde{M} = \tilde{M}_2(\phi)$) while $\beta = \beta(\theta)$, and (iii) GB energy, mobility, and β all are anisotropic, such that $\tilde{M} = \tilde{M}_2(\phi)$. We have taken $r_1 = 1$, $\tilde{S} = 1$, and $\tilde{\tau} = 0$.

stress can also change the direction of misorientation evolution, which in this particular situation would have been towards 0° in the absence of stress. A comparison between Figures 18(a) and 18(b) is also instructive. We note that the misorientation evolution rates are comparatively lower when $\theta_i = 4°$, although the shape evolution remains dominated by the $\dot{\theta}$ dependent term in (2.9).

3.3.3 Effect of anisotropic geometric coupling

Finally, we consider the case when energy, mobility, and coupling factor all are anisotropic. Although the geometric coupling factor $\beta(\theta, \phi)$, given by (2.20), is not differentiable at $\phi = 22.5°$ and 67.5° in $0° \leq \phi \leq 90°$ and $0 \leq \theta \leq \theta_\beta$, the modified stiffness function $B = r_1\tilde{M}_2\tilde{S}/(r_1\tilde{S} + \tilde{M}_2\beta^2)\Gamma_{gb}$ remains smooth. This can be confirmed from the Figure 12. As a result (2.9) remains well-posed. Some illustrations of shape evolution under these conditions are given in Figures 17, 18(a), and 18(b). Here also we see that at the intermediate time instance $\tilde{t} = 0.015$ the shapes are circular, but the shapes are controlled jointly by both the terms in (2.9). In all these cases, anisotropy in β accelerates both the evolution in misorientation angle as well as the shrinkage of the inner grain. In Figure 17, where the shape evolution is dominated by the weighted curvature and hence B, anisotropic β is seen to force the grain to become more round, so much so that the overall evolution has the semblance of isotropy. In Figures 18(a) and 18(b) the shape evolutions are dominated by the $\dot{\theta}$ dependent term in (2.9) and hence we obtain rotated squares at sufficiently large times. The effect of anisotropy in these cases is restricted to affecting the rate of misorientation evolution and the shrinkage.

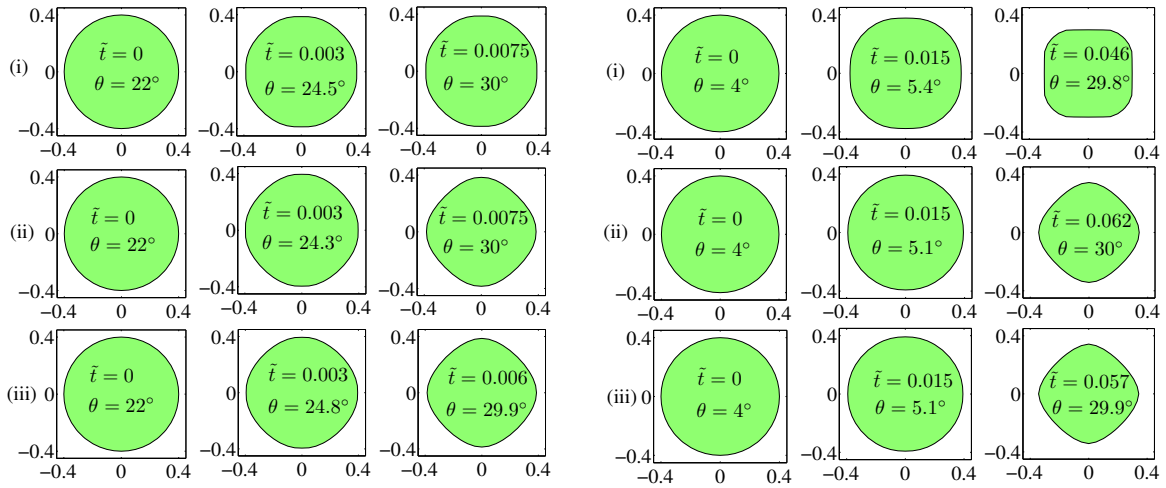

(a) (b)

Figure 18: Evolution of an initially circular GB with (a) $\theta_i = 22°$ and (b) $\theta_i = 4°$ when (i) GB energy is anisotropic, $\tilde{M} = 1$, and $\beta = \beta(\theta)$, (ii) GB energy and mobility are anisotropic ($\tilde{M} = \tilde{M}_2(\phi)$) while $\beta = \beta(\theta)$, and (iii) GB energy, mobility, and β all are anisotropic such that $\tilde{M} = \tilde{M}_2(\phi)$. We have taken $r_1 = 1$, $\tilde{S} = 1$, and $\tilde{\tau} = 6$.

4 Concluding discussion

We have presented a detailed level set method based study of two-dimensional coupled GB motion in a bicrystal. The normal motion of the GB is accompanied by the relative rotation between the grains resulting in the evolution of misorientation. The rotational motion is the manifestation of the biased motion of the atoms in tangential direction of the GB along with normal motion and/or viscous sliding. Our level set simulations have mainly focused on the morphological evolution of the GBs. Initially restricting ourselves to isotropic GB energy and kinetic coefficients we found, among other things, the evolution to slow down for misorientation dependent mobility and sliding coefficients in comparison to the cases when these are constant. We also observed the local minimum in energy (at $\theta = 36.9°$) to introduce a stable fixed point at $\theta = 40.6°$ in the misorientation evolution, while assuming the mode shifting of the coupling factor to be absent. The presence of mode shifting of the coupling factor however brought down the stable fixed point to within the range of misorientation angles in which the mode shifting occurs. The shape evolution of a GB with anisotropic energy was seen to be influenced by both weighted curvature and geometric coupling. Whenever the former dominated the GB dynamics the shape was dictated by Cahn-Hoffman vector plots. The roundness of the shape was then governed by the generalized stiffness which was highest for anisotropic mobility. On the other hand whenever the latter dominated the evolution, the nature of the shape was governed by the symmetry of anisotropic mobility.

One central shortcoming of our approach was regarding the treatment of singularities in the constitutive prescription of GB energy and geometric coupling factor. Our framework required these functions to be sufficiently smooth, which was ensured by using arbitrary smoothening procedures. After doing so however, regardless of the precision in smoothening, there will always exist a possibility of obtaining solutions which could deviate from the physically realizable ones. To solve the governing equations while preserving the nature of singularity will potentially be the most important improvement over the present work. Secondly, because of an explicit numerical scheme (for anisotropic simulations) we had to work with very small time steps for avoiding numerical instability. An implicit or a semi-implicit scheme will possibly allow us to take larger time steps. Finally, we need to have a sufficiently refined mesh for accurate computation of the last integral in the denominator of (2.10). However our use of an explicit time integration scheme restricted us to go below a certain mesh size.

The present study was restricted to two-dimensional GB motion. For its wider application it should be extended to three-dimensional systems including junctions. Presently there is no framework available to model such generalizations. A three-dimensional formulation of GBs will have five degrees of freedom: three misorientation angles and two independent variables describing the GB orientation. The dynamics will be governed by four coupled kinetic relations for normal motion and misorientation evolution. The kinetic coefficients, presently all scalar, will now be higher order tensors. The presence of junctions, on the other hand, will introduce additional kinetic equations for junction velocity and constitutive coefficients such as junction mobility.

References

[1] Gottstein G and Shvindlerman L S 2010 *Grain Boundary Migration in Metals: Thermodynamics, Kinetics, Applications* (CRC Press, Taylor & Francis Group, USA)

[2] Sutton A P and Balluffi R W 2003 *Interfaces in Crystalline Materials* (Clarendon Press, Oxford)

[3] Read W T and Shockley W 1950 *Phys. Rev.* **78** 275–289

[4] Ashby M F 1972 *Surf. Sci.* **31** 498–542

[5] Cahn J W, Mishin Y and Suzuki A 2006 *Acta Mater.* **54** 4953–4975

[6] Cahn J W and Taylor J E 2004 *Acta Mater.* **52** 4887–4898

[7] Taylor J E and Cahn J W 2007 *Interfaces Free Bound.* **9** 493–512

[8] Ramesh K T 2009 *Nanomaterials: Mechanics and Mechanisms* (Springer, USA)

[9] Humphreys F J and Hatherly M 2004 *Recrystallization and Related Annealing Phenomena* (Elsevier, UK)

[10] Li C H, Edwards E H, Washburn J and Parker E R 1953 *Acta Metall.* **1** 223–229

[11] Molodov D A, Ivanov V A and Gottstein G 2007 *Acta Mater.* **55** 1843–1848

[12] Gorkaya T, Molodov D A and Gottstein G 2009 *Acta Mater.* **57** 5396–5405

[13] Legros M, Gianola D S and Hemker K J 2008 *Acta Mater.* **56** 3380–3393

[14] Trautt Z T and Mishin Y 2012 *Acta Mater.* **60** 2407–2424

[15] Trautt Z T, Adland A, Karma A and Mishin Y 2012 *Acta Mater.* **60** 6528–6546

[16] Upmanyu M, Srolovitz D J, Lobkovsky A E, Warren J A and Carter W C 2006 *Acta Mater.* **54** 1707–1719

[17] Bernstein N 2008 *Acta Mater.* **56** 1106–1113

[18] Wan L and Li J 2013 *Modelling Simul. Mater. Sci. Eng.* **21** (055013) 1–22

[19] Warner D H and Molinari J F 2008 *Modelling Simul. Mater. Sci. Eng.* **16** (075007) 1–9

[20] Wu K A and Voorhees P W 2012 *Acta Mater.* **60** 407–419

[21] Osher S and Sethian J A 1988 *J. Comput. Phys.* **79** 12–49

[22] Agnoli A, Bozzolo N, Logé R E, Franchet J, Laigo J and Bernacki M 2014 *Comput. Mater. Sci.* (in press) http://dx.doi.org/10.1016/j.commatsci.2014.03.054

[23] Elsey M, Esedoḡlu S and Smereka P 2009 *J. Comput. Phys.* **228** 8015–8033

[24] Bernacki M, Logé R and Coupez T 2011 *Scr. Mater.* **64** 525–528

[25] Bernacki M, Chastel Y, Coupez T and Logé R 2008 *Scr. Mater.* **58** 1129–1132

[26] Elsey M, Esedoḡlu S and Smereka P 2013 *Acta Mater.* **61** 2033–2043

[27] Hallberg H 2013 *Modelling Simul. Mater. Sci. Eng.* **21** (085012) 1–24

[28] Bernacki M, Resk H, Coupez T and Logé R 2009 *Modelling Simul. Mater. Sci. Eng.* **17** (064006) 1–22

[29] Carlo A D, Gurtin M E and Podio-Guidugli P 1992 *SIAM J. Appl. Math.* **52** 1111–1119

[30] Burger M, Haußer F, Stöcker C and Voigt A 2007 *J. Comput. Phys.* **225** 183–205

[31] Stöcker C and Voigt A 2008 *SIAM J. Appl. Math.* **69** 64–80

[32] Burger M, Stöcker C and Voigt A 2008 *J. Sci. Comput.* **35** 77–98

[33] Rollett A D 2013 Implementation of anisotropic grain boundary properties in mesoscopic simulations *Microstructural Design of Advanced Engineering Materials* ed Molodov D A (Wiley-VCH) pp 161–186

[34] Mullins W W 1957 *J. Appl. Phys.* **28** 333–339

[35] Gurtin M E, Fried E and Anand L 2010 *The Mechanics and Thermodynamics of Continua* (Cambridge University Press, USA)

[36] Gurtin M E 1993 *Thermomechanics of Evolving Phase Boundaries in the Plane* (Clarendon Press, Oxford)

[37] Li J C M 1972 *Surf. Sci.* **31** 12–26

[38] Nazarov A A, Shenderova O A and Brenner D W 2000 *Mater. Sci. Eng. A* **281** 148–155

[39] Upmanyu M 2002 *Scr. Mater.* **56** 553–556

[40] Spencer B J 2004 *Phys. Rev. E* **69** (011603) 1–10

[41] Humphreys F J 1997 *Acta Mater.* **45** 4231–4240

[42] Kazaryan A, Wang Y, Dregia S A and Patton B R 2002 *Acta Mater.* **50** 2491–2502

[43] Mendelev M I, Srolovitz D J, Shvindlerman L S and Gottstein G 2002 *J. Mater. Res.* **17** 234–245

[44] Lobkovsky A E, Karma A, Mendelev M I, Haataja M and Srolovitz D J 2004 *Acta Mater.* **52** 285–292

[45] Gifkins R C 1977 *Metall. Trans. A* **8A** 1507–1516

[46] Watanabe T, Yamada M, Shima S and Karashima S 1979 *Phil. Mag. A* **40** 667–683

[47] Cahn J W, Mishin Y and Suzuki A 2006 *Phil. Mag.* **86** 3965–3980

[48] Suzuki A and Mishin Y 2005 *J. Mater. Sci.* **40** 3155–3161

[49] Moldovan D, Wolf D and Phillpot S R 2001 *Acta Mater.* **49** 3521–3532

[50] Chen Y and Schuh C A 2007 *J. Appl. Phys.* **101** (063524) 1–12

[51] Osher S and Fedkiw R 2003 *Level Set Methods and Dynamic Implicit Surfaces* (Springer-Verlag, New York)

[52] Peng D, Merriman B, Osher S, Zhao H and Kang M 1999 *J. Comput. Phys.* **155** 410–438

[53] Jiang G S and Peng D 2000 *SIAM J. Sci. Comput.* **21** 2126–2143

[54] Chopp D L and Sethian J A 1999 *Interfaces Free Bound.* **1** 1–18

[55] Smereka P 2006 *J. Comput. Phys.* **211** 77–90

[56] Cermelli P and Gurtin M E 1994 *Arch. Ration. Mech. Anal.* **127** 41–99

[57] Fried E and Gurtin M E 2004 *Adv. in Appl. Mech.* **40** 1–177

[58] Gupta A and Steigmann D J 2012 *Math. Methods Appl. Sci.* **35** 1799–1824

[59] Ashby M F and Verrall R A 1973 *Acta Metall.* **21** 149–163

A Derivation of the kinetic relations

The purpose of this appendix is to derive the two-dimensional linear kinetic relations of coupled GB motion as given in Equations (2.9) and (2.10). In order to do so systematically, we start by recalling the basic theory pertaining to kinematics and balance laws. This is followed by a detailed formulation of the dissipation inequality, which is a consequence of the second law of thermodynamics, to subsequently derive the linear kinetic relations within the ambit of linear irreversible thermodynamics. Similar results were previously obtained by Taylor and Cahn [7] using dissipation potentials. Our approach allows us to work in a general framework which can be used to extend the derivation to three-dimensional problems as well as those including deformation in the grain. We will demonstrate these in a separate communication. Our treatment is closer in spirit to that of Gurtin and coauthors [56, 57] but, unlike their method, we avoid postulating an *a priori* existence of configurational forces [58].

A.1 Basic theory

We now collect various kinematical results and balance equations to be used in the following discussion. For further details, including the derivations, we refer the interested readers to a comprehensive account of boundary thermodynamics in [57]. For our purposes, we consider GB as a closed curve C in a two-dimensional section ω of the body, see Figure 19. Let P be some arbitrary part of ω and denote Γ as its intersection with C; we mark a and b as the end points of Γ. We use $\boldsymbol{m}$ to denote the outward unit normal to the boundary ∂P of P, and $\boldsymbol{n}$ and $\boldsymbol{t}$ the unit normal and tangent vectors associated with Γ, as shown in the figure. If $\{\boldsymbol{e}_1, \boldsymbol{e}_2\}$ is a fixed Cartesian basis, with ϕ as the angle between $\boldsymbol{n}$ and $\boldsymbol{e}_1$ (measured anticlockwise from $\boldsymbol{e}_1$), then

$$\boldsymbol{n} = \cos\phi\, \boldsymbol{e}_1 + \sin\phi\, \boldsymbol{e}_2 \text{ and } \boldsymbol{t} = \sin\phi\, \boldsymbol{e}_1 - \cos\phi\, \boldsymbol{e}_2. \tag{A.1}$$

Let $\boldsymbol{x} = \boldsymbol{r}(s,t)$ represent the arc length parametrization of C, where s is the arc length parameter which increases in the direction of $\boldsymbol{t}$. The normal velocity and the curvature are given by (these are

equivalent to the definition in (2.2) and (2.4))

$$V = \frac{\partial \boldsymbol{r}}{\partial t} \cdot \boldsymbol{n} \text{ and } \kappa = \frac{\partial \phi}{\partial s}, \tag{A.2}$$

respectively. The following relations follow immediately from (A.1) and $(A.2)_2$

$$\frac{\partial \boldsymbol{n}}{\partial s} = -\kappa\, \boldsymbol{t} \text{ and } \frac{\partial \boldsymbol{t}}{\partial s} = \kappa\, \boldsymbol{n}. \tag{A.3}$$

A normal trajectory is a smooth curve, passing thorough a point $s = s_0$ on C at time t_0, given by a function $s = S(t)$ such that

$$\boldsymbol{t}(S(t), t) \cdot \frac{d\boldsymbol{r}(S(t), t)}{dt} = 0. \tag{A.4}$$

The normal time derivative of a function $f(s, t)$ defined on C, following the normal trajectory $S(t)$, is defined by

$$\mathring{f}(s, t) = \frac{df(S(\tau), \tau)}{d\tau}\Big|_{\tau=t}. \tag{A.5}$$

It represents the rate of change in f with respect to an observer sitting on C and moving with the normal velocity of the interface. The following relations are easily verifiable (cf. pp. 67-68 in [57]):

$$\mathring{\boldsymbol{t}} = \mathring{\phi}\, \boldsymbol{n},\ \mathring{\boldsymbol{n}} = -\mathring{\phi}\, \boldsymbol{t},\ \mathring{\phi} = \frac{\partial V}{\partial s},\ \text{and } \mathring{\kappa} = \frac{\partial^2 V}{\partial s^2} + \kappa^2 V. \tag{A.6}$$

The end points a and b of Γ lie on curves along ∂P; they can be parametrized with arc length values $S_a(t)$ and $S_b(t)$, respectively such that $\boldsymbol{x}_{a,b} = \boldsymbol{r}(S_{a,b}(t), t)$ (with obvious notation). These are not necessarily normal trajectories at the end points. The normal velocity of the end points, given by $V_{a,b} = \boldsymbol{n}_{a,b} \cdot d\boldsymbol{x}_{a,b}/dt$, is equal to the normal velocity of the curve at the respective points. The tangential endpoint velocity is defined by $W_{a,b} = \boldsymbol{t}_{a,b} \cdot d\boldsymbol{x}_{a,b}/dt$. Here $\boldsymbol{n}_a$ and $\boldsymbol{t}_a$ stand for the normal and the tangent at a, etc. The following identities, with similar ones given at b, are straightforward and will be useful in our subsequent discussion (cf. pp. 69-70 in [57]):

$$\frac{d\boldsymbol{x}_a}{dt} = V_a \boldsymbol{n}_a + W_a \boldsymbol{t}_a \text{ and } \frac{d\phi_a}{dt} = \mathring{\phi}|_a + \kappa_a W_a. \tag{A.7}$$

Assuming zero excess mass density at the GB, the balance of mass requires [57]

$$[\![\rho U]\!] = \frac{\partial h}{\partial s} + [\![\boldsymbol{j}]\!] \cdot \boldsymbol{n} \tag{A.8}$$

at every point on the GB, where h and $\boldsymbol{j}$ denote the diffusional flux along the boundary and in the grain, respectively, ρ is the mass density, and $U^{\pm} = V - \boldsymbol{v}^{\pm} \cdot \boldsymbol{n}$ ($\boldsymbol{v}$ is the material velocity). We have used the notation $[\![f]\!]$ for $(f^+ - f^-)$, where f^+ is the limiting value of f as we approach the boundary from the side into which $\boldsymbol{n}$ points and f^- otherwise. When $[\![\boldsymbol{j}]\!] \cdot \boldsymbol{n} = 0$, we can use (2.8) and $[\![\rho]\!] = 0$ to integrate (A.8) over the entire GB to get [7]

$$h = \frac{\rho \dot{\theta}}{2}(R^2 - \overline{R^2}), \tag{A.9}$$

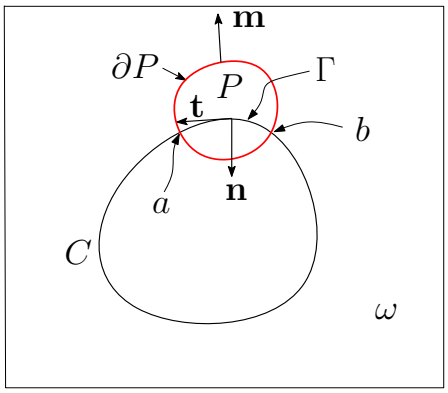

Figure 19: Domain ω containing a GB C.

where $\overline{R^2} = \oint_C R^2 ds/\text{length}(C)$ is the mean square radius of the GB. We have also used the fact that $\dot{\theta}$ is independent of s.

On the other hand, in the absence of body forces, inertia, and surface stress, the balance of linear momentum yields

$$[\![\boldsymbol{\sigma}]\!]\boldsymbol{n} = \boldsymbol{0} \tag{A.10}$$

at every point on the GB, where $\boldsymbol{\sigma}$ is the symmetric Cauchy stress tensor.

A.2 Dissipation inequality

Let Ψ and γ be the free energy densities per unit area of ω and per unit length of C, respectively. The latter is to be understood as an excess quantity in the sense of Gibbs' thermodynamics. We assume body forces and inertial effects to be absent. The mechanical version of the second law of thermodynamics, under isothermal conditions and chemical equilibrium, requires that for any arbitrary part P of ω

$$\int_{\partial P} \boldsymbol{\sigma}\boldsymbol{m}\cdot\boldsymbol{v}ds - \frac{d}{dt}\left(\int_P \Psi da + \int_\Gamma \gamma\, ds\right) \underbrace{- \int_{\partial P} \mu \boldsymbol{j}\cdot\boldsymbol{m}ds - (\mu h)_a^b}_{\alpha} + \underbrace{\left(\boldsymbol{c}\cdot\frac{d\boldsymbol{x}}{dt} + m\frac{d\phi}{dt}\right)_a^b}_{\beta} \geq 0, \tag{A.11}$$

where μ is the chemical potential of the mobile atoms both on the GB and away from it. The left hand side of the inequality gives the total entropy generation within P. The notation $(f)_b^a$ is used for $f_b - f_a$, i.e. for the difference in values of f when calculated at the end points. The first term in the above inequality is the power input into P due to bulk stresses, while the next two terms represent the change in total stored energy content in P. The pair of terms marked with α denote the power input due to the additional mass flow in P [57]. The pair of terms marked as β has to be read as

$$\boldsymbol{c}_b\cdot\frac{d\boldsymbol{x}_b}{dt} - \boldsymbol{c}_a\cdot\frac{d\boldsymbol{x}_a}{dt} + m_b\frac{d\phi_b}{dt} - m_a\frac{d\phi_a}{dt}. \tag{A.12}$$

They represent the power expended due to configurational changes in the portion of the GB contained within P. The exact form of this expression depends on the constitutive prescription of GB energy.

It ensures that the total entropy production at the boundary is given in terms of an entropy density per unit length of the boundary and is independent of the choice of P; this is further elaborated below. The conjugate forces $\boldsymbol{c}$ and m at the end points are determined such that these requirements are maintained. The requirements, it should be noted, are essentially on the nature of excess entropy production and we are free to impose them on the system. The form that the variables $\boldsymbol{c}$ and m take hence depends on the constitutive specification of the GB. Similar considerations, although within a more formal framework of configurations forces, are made in [57], see for e.g. §XVIII therein. Using the surface transport theorem (cf. p. 70 in [57]) and the balance relations (A.8) and (A.10) in (A.11), and by reducing P to a pillbox around Γ, we can obtain

$$\int_\Gamma \left([\![U\boldsymbol{E}]\!] \boldsymbol{n} \cdot \boldsymbol{n} + \tau U_{\tan} - \mathring{\gamma} + \gamma\kappa V - h\frac{\partial \mu}{\partial s} \right) ds + \left(\boldsymbol{c} \cdot \frac{d\boldsymbol{x}}{dt} + m\frac{d\phi}{dt} - \gamma W \right)_a^b \geq 0, \tag{A.13}$$

where $\boldsymbol{E} = (\Psi - \rho\mu)\mathbf{1} - \boldsymbol{\sigma}$ is the Eshelby tensor, $\tau = \boldsymbol{\sigma}\boldsymbol{n} \cdot \boldsymbol{t}$, and $U_{\tan} = [\![\boldsymbol{v}]\!] \cdot \boldsymbol{t}$.

We consider the following regularized form for GB energy [29]

$$\gamma = \gamma_c(\theta, \phi) + \frac{1}{2}\delta_r \kappa^2, \tag{A.14}$$

where $\delta_r \ll 1$ is a constant regularization parameter and γ_c is at least once differentiable w.r.t. θ and twice differentiable w.r.t. ϕ. To evaluate $\mathring{\gamma}$ we use $(\text{A.6})_{3,4}$ with (A.14), in addition to noting that $\mathring{\theta} = \dot{\theta}$ for θ is spatially homogeneous. Its substitution into (A.13), followed by some straightforward manipulation, can be shown to yield

$$\begin{aligned} &\int_\Gamma \left([\![U\boldsymbol{E}]\!] \boldsymbol{n} \cdot \boldsymbol{n} + \tau U_{\tan} + f_{\text{curv}} V - \frac{\partial \gamma_c}{\partial \theta}\dot{\theta} - h\frac{\partial \mu}{\partial s} \right) ds \\ &+ \left[\left(\boldsymbol{c} \cdot \boldsymbol{n} - \frac{\partial \gamma_c}{\partial \phi} + \delta_r \frac{\partial \kappa}{\partial s} \right) V + \left(\boldsymbol{c} \cdot \boldsymbol{t} - \gamma + \delta_r \kappa^2 \right) W + (m - \kappa\delta_r)\frac{d\phi}{dt} \right]_a^b \geq 0, \end{aligned} \tag{A.15}$$

where

$$f_{\text{curv}} = \left(\gamma_c + \frac{\partial^2 \gamma_c}{\partial \phi^2} \right) \kappa - \delta_r \left(\frac{\partial^2 \kappa}{\partial s^2} + \frac{1}{2}\kappa^3 \right). \tag{A.16}$$

The left hand side of (A.15) is the total entropy generation associated with a part Γ of the GB. We would like to choose $\boldsymbol{c}$ and m such that it is expressed in terms of a surface entropy density independent of P, i.e. there exist a density η such that the entropy generation is equal to $\int_\Gamma \eta ds$. As a result we require

$$\boldsymbol{c} \cdot \boldsymbol{n} = \frac{\partial \gamma_c}{\partial \phi} - \delta_r \frac{\partial \kappa}{\partial s}, \ \boldsymbol{c} \cdot \boldsymbol{t} = \gamma_c - \frac{1}{2}\delta_r \kappa^2, \text{ and } m = \kappa\, \delta_r. \tag{A.17}$$

These expressions are in agreement with those obtained in §XVIII of [57]. The dissipation inequality is now reduced to an integral over Γ which, owing to the arbitrariness of Γ, is equivalent to

$$[\![U\boldsymbol{E}]\!] \boldsymbol{n} \cdot \boldsymbol{n} + f_{\text{curv}} V + \tau U_{\tan} - \frac{\partial \gamma_c}{\partial \theta}\dot{\theta} - h\frac{\partial \mu}{\partial s} \geq 0. \tag{A.18}$$

We assume Fick's law for the diffusion flux h, i.e.

$$h = -D\frac{\partial \mu}{\partial s}, \tag{A.19}$$

where $D \geq 0$ is the diffusion mobility along the GB. Recall from Subsection 2.1 that $U_{\tan} = -\dot{\theta}(\boldsymbol{x}\cdot\boldsymbol{n})$, $v_n^+ = \dot{\theta}(\boldsymbol{x}\cdot\boldsymbol{t})$, and $v_n^- = 0$. Using these in (A.18), along with substituting h and $\partial\mu/\partial s$ from (A.9) and (A.19), we can rewrite the dissipation inequality as

$$f_n V + f_{\tan} U_{\tan} \geq 0, \tag{A.20}$$

where

$$f_n = [\![\boldsymbol{E}]\!]\boldsymbol{n}\cdot\boldsymbol{n} + f_{\text{curv}} \text{ and } f_{\tan} = \frac{1}{(\boldsymbol{x}\cdot\boldsymbol{n})}\left(f_s - \frac{\dot{\theta}}{2D_m}\left(R^2 - \overline{R^2}\right)^2\right), \tag{A.21}$$

with $f_s = (\boldsymbol{E}^+\boldsymbol{n}\cdot\boldsymbol{n})\boldsymbol{x}\cdot\boldsymbol{t} + \tau\boldsymbol{x}\cdot\boldsymbol{n} + \partial\gamma_c/\partial\theta$ and $D_m = D/\rho^2$.

Remark A.1 (steady state pure sliding). For the case of steady state pure sliding [59], $V = 0$ and there is no internal entropy generation. With reference to (A.20) this implies $f_{\tan} = 0$ for $U_{\tan} \neq 0$. The following kinetic relation readily emerges from $(A.21)_2$

$$\dot{\theta} = \frac{2D_m \oint_C f_s ds}{\oint_C \left(R^2 - \overline{R^2}\right)^2 ds}. \tag{A.22}$$

If we consider a hexagonal GB and assume $\tau = 0$ then this relation reduces to

$$\dot{\theta} = 60\frac{D_m}{L^5}\oint_C \frac{\partial\gamma_c}{\partial\theta} ds, \tag{A.23}$$

where L is the edge length of the hexagon. This expression matches well with the one obtained recently in [49] except for the constant factor, which was calculated as 95 therein.

A.3 The kinetic relations

The dissipation inequality (A.20) leads us to identify f_n and $f_{\tan}$ as the driving forces for the normal and the tangential motion of the GB, respectively. The simplest kinetic relations for the coupled GB motion can be derived by positing a linear relationship between the driving forces and the velocities, i.e.

$$V = M_{11}f_n + M_{12}f_{\tan} \text{ and} \tag{A.24}$$

$$U_{\tan} = M_{21}f_n + M_{22}f_{\tan}, \tag{A.25}$$

where the coefficients can be at most functions of θ and ϕ. By Onsager's symmetry principle, $M_{12} = M_{21}$. Moreover, dissipation inequality (A.20) requires that the matrix

$$\begin{pmatrix} M_{11} & M_{12} \\ M_{21} & M_{22} \end{pmatrix} \text{ is positive definite.} \tag{A.26}$$

If $M_{11} = 0$ then M_{12} necessarily vanishes so as to satisfy the condition (A.26). The normal motion is then absent and the tangential motion is governed by $U_{\tan} = M_{22} f_{\tan}$ with $M_{22} \geq 0$. The kinetic coefficient M_{22} determines the nature of viscous sliding along the boundary. On the other hand if $M_{11} \neq 0$ the kinetic relations can be rewritten in the form

$$U_{\tan} = \beta V + S f_{\tan} \text{ and} \tag{A.27}$$

$$V = M f_n + M \beta f_{\tan}, \tag{A.28}$$

where $S = M_{22} - M_{12}^2/M_{11}$, $M = M_{11}$, and $M_{12} = \beta M$ (when $M \neq 0$).

For simple GB migration $f_{\tan} = 0$ and $U_{\tan} = 0$, reducing the kinetic relations to the familiar equation $V = M f_n$; the coefficient M therefore has the physical interpretation of GB mobility [1,9]. For a purely tangential motion the kinetic relations reduce to $U_{\tan} = S f_{\tan}$; the coefficient S hence represents the pure viscous sliding coefficient [5, 7]. Furthermore, when $f_{\tan} = 0$, $V = M f_n$ and $U_{\tan} = \beta V$. This implies that, even when the tangential driving force is absent, the grains can move in a tangential direction w.r.t. the GB due to the coupling between the normal and the tangential motion. The coupling coefficient β, which turns out to be a geometrical quantity, has been a subject of much interest in the recent theoretical and experimental literature [5, 11, 12]. Substituting (A.27) and (A.28) back into (A.20), we obtain

$$M(f_n + \beta f_{\tan})^2 + S f_{\tan}^2 \geq 0, \tag{A.29}$$

according to which M and S are required to be strictly non-negative.

The kinetic relation for the normal velocity, given in (2.9), is obtained by replacing $f_{\tan}$ in (A.28) from (A.27). The other kinetic relation (2.10), for the evolution of misorientation θ, is derived by first substituting V from (A.28) into (A.27) and then integrating the equation over the closed GB. Recall that the misorientation angle is independent of s and depends only on time t.

Remark A.2. There are two differences in our expressions for the kinetic laws in comparison to those derived by Taylor and Cahn [7]. In expression (2.10) for $\dot{\theta}$ their formula has a positive sign, compared to the negative sign in (2.10), before the last term in the denominator. In the same term there is also a mismatch of factor of 2. The negative sign in our expression is justified for it leads to the correct expression for sliding rate in the case of steady state pure sliding (see Remark A.1). Secondly, the expression for $\dot{\theta}$ in [7] contains an additional term in the denominator, which appears due to their choice of dissipation functional.

B Role of elasticity of the grains

We present a small calculation to justify why we can neglect elastic deformation of the grains in our present work. We consider the bicrystal of Section 2 with a circular GB of initial radius R_i undergoing a purely normal motion due to its curvature. The driving force f_n, which can be seen

as a pressure on the outer surface of the inner grain, is given by γ_c/R_i, where γ_c is the GB energy introduced in Section 2. To calculate a typical value for the total dissipation rate during migration, we take $R_i = 20\text{nm}$, constant mobility $M_0 = 10^{-7}\text{m}^4/\text{J/s}$ [14], and GB energy $\gamma_c = 0.76\text{J/m}^2$. The energy has been evaluated using shear modulus $\mu = 46\text{GPa}$, Poisson's ratio $\nu = 0.34$, and $\theta = 15^\circ$ in (2.11). The total dissipation rate at $t = 0$ is $D_c = \pi f_n V R_i^2 = 18\text{J/s}$ per unit axial length of the GB. On the other hand, we compute the rate of change of total elastic energy of the inner grain under the influence of a hydrostatic pressure of similar magnitude as of f_n. We take the inner grain to be a solid cylinder of length L with one end fixed, while keeping the the other traction free. Assuming the material response to be isotropic and the problem to be axisymmetric, we can calculate the total strain energy rate at $t = 0$ as $\dot{W}_c \approx \big(\pi M \gamma_c^3(\lambda + 2\mu)\big) \,/\, \big(2\mu R_i^2(3\lambda + 2\mu)\big)$ per unit axial length of the GB, where λ is a Lame constant. Substitution of various constants yields $\dot{W}_c = 1.8 \times 10^{-3}$ J/s per unit axial length of the GB. A comparison between the order of the magnitudes of the dissipation rate and the rate of change of elastic energy will readily justify our assumption to neglect elasticity of the grains. Even the inclusion of tangential shear in the grains will not change the order of the net elastic energy rate significantly.